Description and performance of the UIUC 24-layer stratosphere/troposphere general circulation model

Fanglin Yang,[1] Michael E. Schlesinger, and Eugene Rozanov

Climate Research Group, Department of Atmospheric Sciences, University of Illinois at Urbana-Champaign, Urbana

Abstract. This paper describes the 24-layer stratosphere/troposphere general circulation model (24-L ST-GCM) developed by the Climate Research Group of the University of Illinois at Urbana-Champaign (UIUC). The model's dynamical and physical processes, similar to those of its ancestors, are briefly described. The newly implemented parameterizations of longwave and solar radiation, cloud-radiation interaction, subgrid-scale orographic gravity wave drag, and aerosol radiative forcing are described in more detail. Sensitivity tests using simplified one-dimensional column models and the 24-L ST-GCM are carried out to evaluate these implementations. A 15-year simulation with prescribed climatological sea-surface temperatures and sea-ice extents has been performed. To determine the model's strengths and weaknesses, the simulated results are compared with observations. The model simulates well the geographical distributions of surface-air temperature and precipitation and their seasonal variations. The simulated cloud cover and cloud radiative forcing have the observed magnitudes and latitudinal variations, except near 60°S where the model underestimates the cloud cover by ~20-30%. It is found that the large-scale cloud distribution and the cloud-top altitude depend on the respective critical relative humidities for the onset of large-scale precipitation and penetrating convection. The model captures reasonably well the observed features of atmospheric temperature and zonal wind in both the stratosphere and troposphere in all seasons, with the exception of the northern stratospheric polar-night jet. The simulated Transformed-Eulerian-Mean residual circulation in the stratosphere has comparable magnitudes and distributions to those obtained by data assimilation and other general circulation models (GCMs). The two-cell Brewer-Dobson circulation is captured. The use of an orographic-type gravity wave drag parameterization is responsible for an abnormally warm northern polar stratosphere in winter, which is contrary to most other GCMs.

1. Introduction

A fundamental goal of atmospheric research is to understand past, present, and potential future climates using comprehensive numerical general circulation models (GCMs) of the atmosphere. Atmospheric GCMs (AGCMs) have been under development for the past three decades, but most either do not extend higher than the lower stratosphere or have only a coarse resolution in the stratosphere. These "lower-atmosphere" GCMs have provided understanding of the potential climate changes induced by increasing greenhouse gases (GHGs). However, to understand the influence of GHG-induced climate change on the Earth's protective ozone shield and, conversely, the effect of ozone changes on climate requires a GCM that resolves the stratosphere well and possibly even the mesosphere. A few research centers and university groups in the world have been developing such troposphere/stratosphere or troposphere/stratosphere/mesosphere GCMs, based either on their existing tropospheric GCMs or

troposphere/lower-stratosphere GCMs. Such models include, for example, the Geophysical Fluid Dynamics Laboratory's (GFDL) "SKYHI" GCM [*Hamilton et al.*, 1995], the middle-atmosphere version of the National Center for Atmospheric Research (NCAR) Community Climate Model (MACCM2) [*Boville*, 1995], the Goddard Institute for Space Studies' (GISS) Middle Atmosphere Model [*Rind et al.*, 1988a, b], the United Kingdom Meteorological Office's (UKMO) Unified Model [*Cullen*, 1993; *Swinbank et al.*, 1998], the Max Planck Institute for Meteorology's ECHAM3.5 model [*Manzini and Bengtsson*, 1996], the Berlin troposphere-stratosphere-mesosphere GCM [*Langematz and Pawson*, 1997], and the Canadian Middle Atmosphere Model [*Beagley et al.*, 1997].

A 24-layer stratosphere/troposphere general circulation model (24-L ST-GCM) has been under development by the Climate Research Group of the University of Illinois at Urbana-Champaign (UIUC) since 1994. The main purposes of developing this model are to (1) couple it with our photochemical model to simulate and understand ozone photochemistry and greenhouse-gas-induced climate change and their interactions and (2) study the radiative forcing and climate changes induced by volcanic eruptions. Given limited computing resources and our primary interest in the dynamics, physics, and chemistry of the troposphere and the stratosphere, we put the top of the model at the stratopause.

Before any GCM is used to study climate changes, it should be validated. Performing a long-term climate simulation with prescribed present external forcing and boundary conditions

---

[1]Now at National Center for Environmental Prediction, Washington, D.C.

for the atmosphere and comparing the simulated model results with observed present climate have been the standard practice of validation adopted by the climate-modeling community for decades. It is also essential to document important changes made to a GCM, the influence of those changes, the strength and weakness of the resulting model, and their causes. This type of documentation serves as a reference for future development of the model and for understanding the simulated features of a perturbed climate when the model is applied to study climate changes. Accordingly, many papers have been published that focused on the validation and documentation of GCMs. For example, the references listed above are all dedicated to the purposes of model documentation and validation, although they focused on different aspects of their GCMs.

The UIUC 24-L ST-GCM has been coupled with an atmospheric chemical-transport model (ACTM) in an off-line mode to simulate the distributions of source gases and ozone in the stratosphere [Rozanov et al., 1999a, b]. It has also been used to reconstruct the radiative forcing of historical volcanic eruptions [Andronova et al., 1999], to simulate climate changes induced by the Mount Pinatubo volcanic eruption [Yang, 2000], and to perform a 17-year transient climate simulation for the Second Atmospheric Model Intercomparison Project (AMIP-II) [Gleckler, 1999]. However, it was not appropriate to give a full description of the 24-L ST-GCM in the papers cited above. Therefore it is of considerable interest to document the model's structure and describe the quality of its simulation of the present climate. These are the objectives of the present paper.

The plan of this paper is as follows. In section 2 the 24-L ST-GCM is described, and the results of some sensitivity tests are presented. The model's finite-difference schemes and treatments of unresolved-scale physical processes such as precipitation, boundary layer processes, radiative transfer, and gravity wave drag are described. We focus on the newly implemented radiative-transfer and gravity wave drag parameterizations since detailed descriptions of the model's dynamics, precipitation, and boundary layer processes are given by Oh [1989] and Ghan et al. [1982]. Sensitivity experiments are performed using simplified one-dimensional (1-D) column radiative-transfer models to compare the heating and cooling rates between the new and old radiative routines. Two perpetual January simulations are presented to study the influence of the parameterization of subgrid-scale orographic gravity wave drag on the simulated circulation and sea level pressure field. Section 3 presents first the basic model climatology from a 15-year control simulation with prescribed climatological sea-surface temperatures and sea-ice extents and its comparison with observations and then the simulated residual circulation in the stratosphere. A summary and discussion of the model's performance are presented in section 4.

2. Model Description and Sensitivity Studies

The 24-L ST-GCM is a descendent of the two-layer atmospheric GCM developed in the late 1960s and early 1970s by A. Arakawa and Y. Mintz at UCLA [Gates et al., 1971] and subsequently developed by M. E. Schlesinger and used by Schlesinger and Zhao [1989] and Schlesinger and Verbitsky [1996]. Beginning in 1984, M. E. Schlesinger and J. H. Oh developed a multilayer (ML) version of the AGCM. The original seven-layer tropospheric version of this ML-AGCM was used by Oh for his Ph.D. research at Oregon State

University to develop and test a physically based parameterization of clouds and their radiative interactions [Oh, 1989]. Since 1989 the ML-AGCM has been revised in several ways, and 11-layer troposphere/lower stratosphere [Wang, 1996; Schlesinger et al., 1997a; Wang and Schlesinger, 1999] and 24-layer stratosphere/troposphere versions of the model have been developed.

The architecture of the 24-L ST-GCM, as well as that of the seven-layer and 11-layer AGCMs, and their numerical code for integrating the primitive equations is the same as for the two-layer AGCM [Gates et al., 1971; Ghan et al., 1982]. The seven-layer AGCM, with its top at 200 hPa, differs from the two-layer AGCM mainly in its vertical resolution and the treatment of radiation, clouds, precipitation, and the planetary boundary layer [Oh, 1989]. The 11-layer AGCM, with its top at 50 hPa, possesses the same dynamic and physical features as the seven-layer AGCM but is significantly improved in simulating the present climate, especially the tropical intraseasonal oscillation [Wang and Schlesinger, 1995; Wang, 1996; Wang and Schlesinger, 1999]. For the 24-L ST-GCM new parameterizations have been developed for the transfer of both terrestrial radiation and solar radiation. The interaction between clouds and radiation has also been modified. The radiative effects of aerosols in both the troposphere and stratosphere have been included. A parameterization scheme for orographically excited subgrid-scale gravity wave drag has been included in the model. The 24-L ST-GCM is described below in terms of (1) its predicted quantities and solution methods and (2) its parameterizations, the treatment of its unresolved-scale physical processes.

2.1. Predicted Quantities and Numerical Solution Methods

The model prognostically calculates the velocity, temperature, water vapor mixing ratio and cloud water amount for 24 specified vertical layers in the atmosphere, together with the surface pressure, ground temperature, soil water, and snow mass and diagnostically calculates many other quantities, including the temperature and water vapor content of the surface air (2 m above the ground), the cloud droplet number concentration and cloud amount, and the rainfall and snowfall. In the version of the 24-L ST-GCM coupled to our ACTM with interactive photochemistry, many chemical species are also prognostic variables [Rozanov et al., 1999a, b].

The horizontal distribution of dependent variables in the model is staggered according to the B grid to simulate the process of geostrophic adjustment [Arakawa and Lamb, 1977], and the model uses finite differences that conserve the total atmospheric mass, total energy under adiabatic and frictionless motion, and enstrophy (mean square vorticity) for the nondivergent component of the wind field [Arakawa, 1966]. The model's grid is latitude-longitude, with a 4° by 5° resolution (Figure 1).

Vertically the model extends from the Earth's surface to 1 hPa (Figure 2). The model uses sigma (σ) as its vertical coordinate, such that the Earth's surface is the coordinate surface $\sigma = 1$ and the top of the model is the coordinate surface $\sigma = 0$. The structure of the vertical layers was chosen to (1) resolve the peak of the ozone concentration around 10 hPa, (2) eliminate internal wave reflection and overcome computational modes [Tokioka, 1978], and (3) represent well the planetary boundary layer. The pressure values at half-integer levels in the first 10 layers in the upper atmosphere follow $p_{k+1/2} = p_{k-1/2} e^d$, where d = (ln$p_{10+1/2}$−ln$p_T$)/10, $p_T = p_{1/2} = 1$ mb,
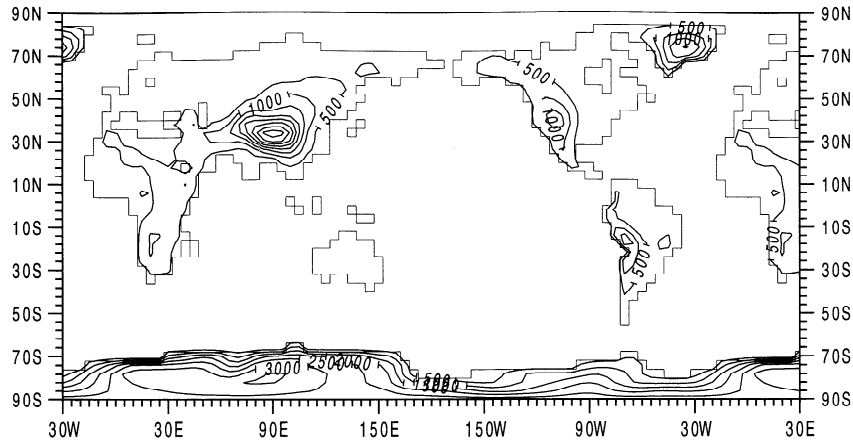
Figure 1. The continental outline and surface elevation (m) of the UIUC 24-L ST-GCM, with 4° latitude by 5° longitude resolution. The contour interval for the surface elevation is 500 m. The primary grid is centered at latitudes ±2°, ±6°, ... and longitudes 0°, ±5°, ...
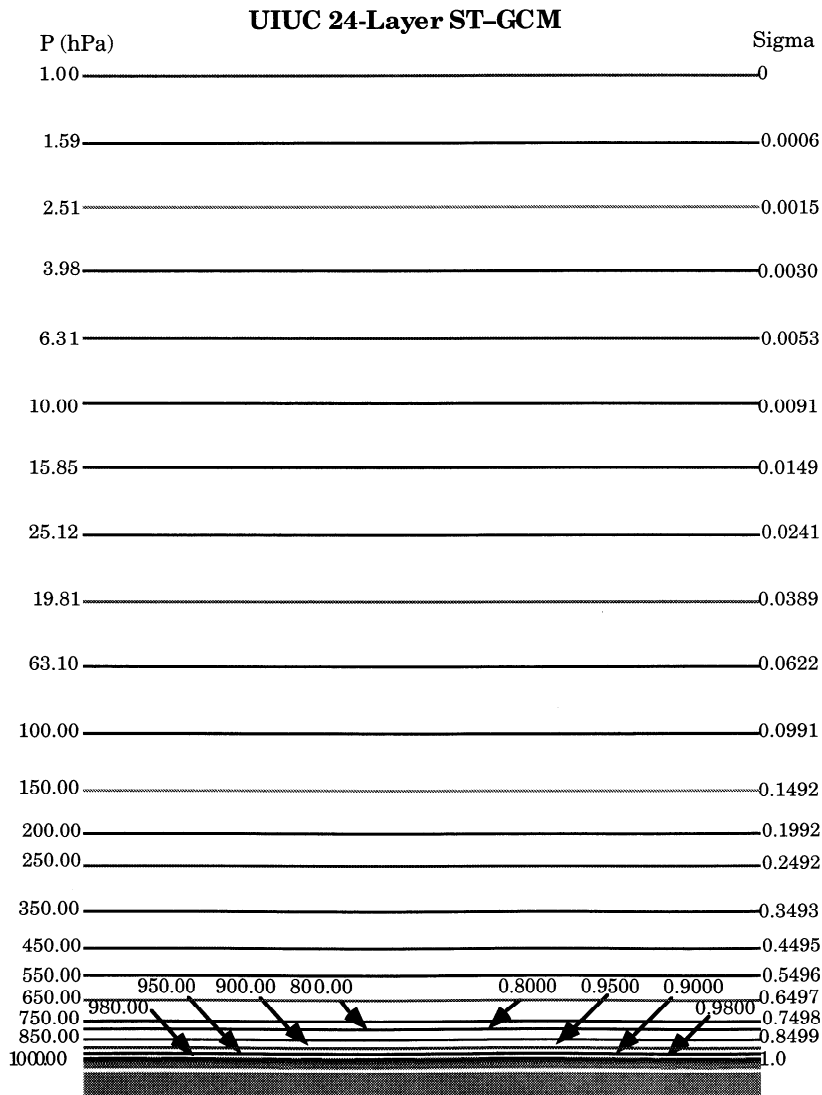

Figure 2. The vertical structure of the UIUC 24-L ST-GCM.

$p_{10+1/2} \approx 100$ mb, and k enumerates the layers downward from the top layer of the model, $k=1$, to the 10th layer. There are 14 model layers from ~100 hPa to the Earth's surface with preset pressure values for a given surface pressure of 1000 hPa (Figure 2).

The adiabatic and frictionless terms in the primitive equations and in the conservation equations for water vapor and cloud water/ice are integrated in time using a sequence of 10 steps per simulated hour, comprised of six time-alternating space-uncentered (TASU) steps with the Matsuno scheme and four space-centered steps with the leapfrog scheme. The diabatic and frictional terms in these equations are evaluated once per simulated hour. To avoid having to reduce the timestep to maintain linear computational stability in high latitudes where the meridians converge, a longitudinal smoothing of the zonal pressure gradient and the zonal mass flux is performed poleward of 34° latitude. This time integration of the model requires ~75 hours of Cray C-90 computer time per simulated year.

2.2. Parameterizations: Treatment of Unresolved-Scale Physical Processes

Owing to computational constraints, there are many unresolved-scale (subgrid-scale) physical processes whose effects on the resolved-scale quantities are calculated in terms of those quantities alone; that is, they are parameterized. These are described below for (1) the surface and planetary boundary layer, (2) subgrid-scale transports, convection, large-scale condensation, precipitation, and cloud, (3) radiative transfer, (4) aerosols, and (5) gravity wave drag. A more detailed description of parameterizations (1) and (2) is given by *Oh* [1989].

2.2.1. Surface and planetary boundary layer.
The topography of the model is that obtained by area-averaging 1°x1° topography [*Gates and Nelson*, 1975] over each of the model's 3312 4°x5° grid cells (Figure 1). The surface roughness length over land is taken as the maximum of a function of the standard deviation of the topography [*Fiedler and Panofsky*, 1972] and the roughness length of the local vegetation, including a "zero plane displacement" value for tall vegetation types [*Monteith*, 1973]. Over sea ice, the roughness length is constant [*Doronin*, 1969]. Over ocean, the roughness is a function of the surface wind speed. In the version of the model in which sea-surface temperature and sea-ice extent are not calculated, their distributions are prescribed from the AMIP-II climatology. In the version of the model in which sea-surface temperature and sea-ice extent are calculated, they are done so by a fixed-depth, 60 m, mixed layer ocean model, and a thermodynamic sea-ice model.

The turbulent surface fluxes of momentum, sensible heat, and moisture are parameterized by bulk formulas that depend on the differences of the momentum, temperature, and moisture between the ground and surface air, the surface-air wind speed, and aerodynamic drag and transfer coefficients. The surface-air wind is taken as a fraction of the winds extrapolated from the lowest two model layers. For comparison with observations, sea level pressure, surface-air temperature, and geopotential height and temperature below ground are diagnosed following *Trenberth et al.* [1993]. The surface-air moisture is taken to be the same as that at the lowest atmospheric level (Figure 2). The aerodynamic drag and transfer coefficients depend on the vertical stability and surface roughness length, with the same transfer coefficient used for the fluxes of sensible heat and

moisture. The surface moisture flux depends on evapotranspiration efficiency, taken as unity over snow, ice, and water and as a function of the soil wetness over land.

The ground temperature is taken to be the average temperature over the diurnal skin depth, calculated from a prognostic budget equation whose source and sink terms include the surface fluxes of radiation, sensible heat and latent heat, and the heat transfer into the ground. The latter depends on the thermal conductivity and bulk heat capacity of the ground.

The soil wetness is determined from a prognostic budget equation that includes the rates of precipitation, snowmelt, surface evaporation, and runoff. Soil wetness is the ratio of the soil moisture content to the field capacity, the latter prescribed for each of the 35 combinations of the AGCM's five soil textures (sandy, sandy loam, light loam, loamy, and heavy loam, clay) and seven surface types (evergreen wood and forest, mixed and deciduous wood and forest, grassland, cropland, shrub and semi-desert, desert, and tundra, mountain, arctic flora) [*Vinnikov and Yeserkepova*, 1991]. The evapotranspiration efficiency over land is taken as the minimum of 4/3 the soil wetness and unity. The runoff rate is a nonlinear function of the soil wetness and the combined rates of precipitation and snowmelt. If the predicted soil wetness exceeds unity, the excess moisture is taken as additional runoff.

The snow mass is determined from a prognostic budget equation that includes the rates of snow accumulation, melting, and sublimation. Precipitation falls as snow if the temperature for the lowest model layer is less than 0°C. The snowmelt rate is computed over land from the difference between the downward heat fluxes at the surface and the upward heat fluxes that would occur for a ground temperature equal to the melting temperature of snow (0°C). Snowmelt contributes to the soil moisture. Accumulation and melting of snow may also occur on sea ice. The surface sublimation rate is equated to the evaporative flux from snow, unless sublimation removes all the snow mass in less than 1 hour, in which case the sublimation rate is set equal to the snow mass removal rate.

The dependence of the albedo of snow-covered surfaces on zenith angle and snow temperature has been included in the model following *Briegleb and Ramanathan* [1982]. The seasonal variation of the albedo of snow-free surfaces is prescribed from the observational data compiled by *Matthews* [1983]. Surface albedo has been made a linear function of the snow-covered and snow-free albedo, weighted by a function of snow depth and surface roughness. The top of the planetary boundary layer (PBL) is taken to be the height of the lowest four atmospheric layers (Figure 2). Cloud in the PBL is diagnostically computed on the basis of a cloud-topped mixed layer model [*Guinn and Schubert*, 1989; *Lilly*, 1968].

2.2.2. Subgrid-scale transports, convection, large-scale condensation, precipitation, and clouds.
The model has parameterized stability-dependent, subgrid-scale turbulent vertical transports of heat, water vapor, and horizontal momentum. There are no subgrid-scale turbulent horizontal transports of these quantities. A momentum drag is included in the top layer of the model that is proportional to air density and the square of the velocity [*Hansen et al.*, 1983].

The model has three parameterizations for convection: (1) dry-convective adjustment, (2) middle-level convection, and (3) penetrating convection. Dry-convective adjustment occurs if the temperature lapse rate between any two adjacent vertical layers is absolutely unstable, that is, exceeds the dry-adiabatic lapse rate. Middle-level convection occurs if the

temperature lapse rate between any two adjacent vertical layers is conditionally unstable and the lower-layer air is sufficiently near saturation that it would be positively buoyant if displaced to the higher layer [*Arakawa*, 1969; *Arakawa and Mintz*, 1974]. Penetrating convection occurs if the temperature lapse rate between the PBL and any layer above is conditionally unstable and the PBL air is sufficiently near saturation that it would be positively buoyant if displaced to the higher layer [*Arakawa and Schubert*, 1974].

Large-scale condensation occurs in a layer not only when the grid cell is everywhere saturated but also when only part of the grid cell is saturated [*Sundqvist*, 1978; 1988]. The rate of condensation depends on the large-scale convergence rates of moisture, heat, and mass and the time rate of change of fractional relative humidity of the layer, U. The latter is determined from $U = bU_s + (1-b)U_0$, where b is the fractional cloudiness, U_s (=100.6%) is the supersaturated relative humidity within the cloud, $1-b$ is the cloud-free fraction, and U_0 is the fractional relative humidity of the clear air. Closure is achieved by assuming (1) the moisture convergence is partitioned between the cloud and clear air in proportion to b and $1-b$, respectively and (2) $U_0 = U_{00} + b(U_s - U_{00})$, where U_{00} is the relative humidity at which condensation can begin. The result is that $b = 1 - [(U_s - U)/(U_s - U_{00})]^{1/2}$, which increases from zero for $U = U_{00}$ to unity for $U = U_s$. U_{00} is taken to be 98%.

For clouds with temperature below 0°C, a fraction of the prognostically calculated cloud water is taken to be ice, with the fraction increasing linearly from zero at 0°C to unity at −30°C. Precipitation occurs in the ice phase if the cloud temperature is less than 0°C and in the liquid phase otherwise. The rate of cloud-water conversion to precipitation is 10 times larger for the ice phase than for the liquid phase. Large-scale precipitation beneath cloud base evaporates (sublimates) at a rate that is proportional to the product of the precipitation rate, the relative humidity deficit from saturation, and the cloud-free fraction of the grid cell. Convective precipitation beneath cloud base evaporates at a rate that is proportional to the product of the relative humidity deficit and the cloud-water content [*Schlesinger et al.*, 1988].

Stratiform and cumuloform clouds can coexist within the same vertical atmospheric column, albeit not in the same layer. A cloud in any vertical layer is identified as either a stratiform or cumuloform cloud depending on the preceding cloud type, the large-scale condensation, and the convective mass flux in the layer. If there is convective mass flux, the cloud type is taken to be cumuloform regardless of whether the preceding cloud was stratiform or cumuloform. If there is large-scale condensation and no convection, the cloud is taken to be stratiform. If there is neither convection nor large-scale condensation, the cloud maintains its cloud type until it dissipates by evaporation [*Schlesinger and Oh*, 1993].

2.2.3. Radiative transfer and radiation-cloud interaction. When we created the first version of the 24-L ST-GCM from our 11-layer tropospheric GCM [*Wang and Schlesinger, 1995; Schlesinger et al., 1997a; Wang and Schlesinger, 1999*], we employed the radiative parameterization of the latter [*Oh*, 1989] (hereafter UIUC89). However, that parameterization proved to be unsatisfactory for the stratosphere in the ST-GCM. Inaccurate longwave cooling and solar heating prohibited the model from being integrated forward longer than a month before the model suffered computational instability because of unrealistically strong winds. Accordingly, as

described below, we have developed new parameterizations (hereafter UIUC98) for terrestrial (infrared) and solar radiation and their interaction with clouds.

2.2.3.1. Terrestrial radiation. The UIUC98 parameterization of infrared radiation is based on the parameterization developed by *Chou and Suarez* [1994] which computes absorption and emission of terrestrial radiation due to water vapor, carbon dioxide, and ozone and contains eight broadbands ranging in wavenumber from 3000 to 0 cm^{-1}. The third band (~540-800 cm^{-1}) contains three subbands to cover the rapid changes of the CO_2 absorption coefficients between the band center and band wings. Depending upon the importance of the scaling effect of the vertical variations of pressure and temperature on absorption, three different approaches are used to compute the transmission functions for different gaseous absorbers: (1) the k distribution method with linear pressure and/or temperature scaling, (2) two-parameter scaling with precomputed look-up tables, and (3) one-parameter scaling. *Chou and Suarez* [1994] examined and validated this parameterization against accurate line-by-line calculations. They showed that the scheme is capable of computing the cooling rate accurately for both the middle and lower atmospheres (from 0.01 hPa to the surface) with errors less than 0.4°C d^{-1}.

To use the *Chou and Suarez* [1994] parameterization in the 24-L ST-GCM, we have modified the parameterization to take into account the influence of clouds, aerosols, and trace gases (N_2O, CH_4, CFC-11, CFC-12, and HCFC-22) according to M.-D. Chou (personal communication, 1997). In this UIUC98 version, two-parameter scaling is used for absorption by the centers of the water vapor bands, the k distribution method with linear pressure scaling is used for absorption by the wings of the water vapor bands, and one-parameter temperature scaling is used for the water vapor continuum absorption. Two-parameter scaling is also used to compute CO_2 and O_3 absorption because Doppler broadening of their absorption lines is important in the upper stratosphere. The transmittances due to trace gases are computed using the k distribution method with linear pressure scaling. A narrow band in the 15 μm region has been added to account for the flux reduction due to N_2O. The sixth band (1100-1380 cm^{-1}) in the *Chou and Suarez* [1994] parameterization has been divided into two bands (M.-D. Chou, personal communication, 1997). Table 1 shows the longwave spectral bands, together with the corresponding absorbers and methods of computing transmittance. To reduce computing time the column-integrated absorber amount and absorber-weighted temperature and pressure are assumed not to change within each simulated 6-hour period; thus the transmission functions due to gaseous absorbers are computed only 4 times per day.

To illustrate the importance of this revision of the longwave radiation parameterization in correctly simulating the atmospheric cooling rate, a column radiative-transfer model was constructed using the infrared radiation scheme of our seven-layer tropospheric and 11-layer troposphere/lower-stratosphere GCMs (UIUC89) [*Oh*, 1989], and a second radiative-transfer model was constructed using the new infrared radiation scheme (UIUC98) described above. Both of the 1-D column models extend up to 1 hPa and have identical 24 layers, with sigma values prescribed to be the same as in the 24-L ST-GCM (Figure 2). With the initial profiles of temperature, pressure, ozone, and water vapor interpolated from the standard atmosphere of *McClatchey et al.* [1972] to the model layers and with only the major contributors to longwave

Table 1. Longwave Spectral Bands With Corresponding Absorbers and Methods Used to Compute Transmittances

Band	Wavelength, cm^{-1}	Absorber	Transmittance Calculation Method
1	0-340	H_2O line	two-parameter
2	340-540	H_2O line	two-parameter
3	540-800	H_2O & 15 μm CO_2 overlap	k distribution
		H_2O continuum	one-parameter
		CO_2	two-parameter
		N_2O	k distribution
4	800-980	H_2O line	k distribution
		H_2O continuum	one-parameter
		CO_2	k distribution
		CFC-11, CFC-12, HCFC-22	k distribution
5	980-1100	H_2O line	k distribution
		H_2O continuum	one-parameter
		O_3	two-parameter
		CO_2 and CFC-11	k distribution
6	1100-1215	H_2O line	k distribution
		H_2O continuum	one-parameter
		N_2O, CH_4	k distribution
		CFC-12, and HCFC-22	k distribution
7	1215-1380	H_2O line	k distribution
		H_2O continuum	one-parameter
		N_2O and CH_4	k distribution
8	1380-1900	H_2O line	two-parameter
9	1900-3000	H_2O line	k distribution

Revised from Table 1 of *Chou and Suarez* [1994]

cooling (H_2O, CO_2, and O_3) included, the cooling rates (°C d^{-1}) are computed for the clear-sky atmospheric conditions of midlatitude summer, tropics, and subarctic winter, separately using the two 1-D radiative-transfer models. Here the CO_2 concentration is taken to be 350 ppmv throughout the atmosphere. Cooling rates (negative) computed from these two models and their differences (UIUC98 minus UIUC89) are presented in Figure 3 for the four atmospheric conditions. It is seen from Figure 3 that the UIUC89 longwave parameterization is not accurate relative to the UIUC98 parameterization. For the cases of midlatitude summer and tropics it overestimated the cooling rates in the stratosphere, with the largest error of ~2°C d^{-1} occurring in the middle stratosphere near 10 hPa, and underestimated the cooling rates in the troposphere, except near the surface, with the largest error of ~1.2°C d^{-1} occurring near 200 hPa. For the case of subarctic winter, the UIUC89 longwave parameterization slightly underestimated the cooling rate in the middle troposphere, but severely overestimated the cooling rate in the upper stratosphere, with a maximum error reaching 4.8°C d^{-1}.

The effects of clouds on terrestrial radiation are included in the UIUC98 parameterization by introducing a mean flux transmittance which is the product of the gaseous transmit-

tances and a cloud-related coefficient [*Chou and Suarez*, 1994]. This coefficient is calculated for each GCM layer and conveys information about cloudiness, cloud optical thickness, and cloud overlapping. This approach is flexible enough to allow the choice of the type of cloud overlapping to be used. To be consistent with the solar-radiation parameterization, clouds are grouped into three categories: high clouds above the 16th σ layer (~ 400 hPa) of the model, middle clouds between the 16th and 19th σ layers (~ 700 hPa), and low clouds below the 19th σ layer (see Figure 2). Clouds within each category are assumed to be maximally overlapped, while the different cloud categories are assumed to be randomly overlapped. The cloud transmission function for a given layer depends on the prognostically calculated cloud liquid and/or ice water path and cloud emissivities, with the latter prescribed following *Stephens* [1978] for liquid-water clouds and *Starr and Cox* [1985] and *Griffith et al.* [1980] for ice clouds.

2.2.3.2 Solar radiation. The UIUC98 parameterization of solar radiation is based on the parameterization developed by *Chou* [1990, 1992], *Chou and Lee* [1996], and *Chou and Suarez* [1999]. We have added the scattering and absorption of aerosols and modified the cloud-radiation interaction. The UIUC98 parameterization computes the absorption by water vapor, ozone, carbon dioxide, oxygen, clouds and aerosols, and the scattering by clouds, aerosols and molecules (Rayleigh scattering). There are eight bands in the ultraviolet and visible spectral regions (0.175-0.7 μm) and three bands in the near-infrared and thermal-infrared regions (0.7-10.0 μm) (Table 2). In the first eight bands, effective coefficients for ozone absorption and effective cross sections for Rayleigh scattering are precomputed. In each of the last three bands, the k distribution method with simple pressure scaling is used to calculate the solar heating by water vapor and carbon dioxide. Absorption and scattering of solar radiation by clouds are included in all 11 spectral bands (0.175-10 μm).

Cloud grouping and overlapping are treated in the same way as in the longwave-radiative transfer parameterization. The shortwave-radiative properties of liquid-water clouds [*Slingo*, 1989] depend on liquid-water path and the equivalent radius of the drop-size distribution (r_e), the latter determined by the prognostically calculated cloud liquid-water content and the diagnostic cloud-droplet number concentration (CDNC). The CDNC is empirically related to the sulfate aerosol mass concentration [*Boucher and Lohmann*, 1995]. This approach enables us to study the indirect radiative forcing of sulfate aerosol. Shortwave radiative properties of ice clouds are also functions of the ice-water path and ice crystal effective size, taken to be 70 μm. For mixed phase clouds, the optical depth is the summation of water-cloud optical depth and ice-cloud optical depth, the single-scattering albedo is optical-depth weighted, and the asymmetry factor is optical-depth and single-scattering albedo weighted. The delta-Eddington method is first used to calculate transmittance and reflectance of each layer [*King and Harshvardhan*, 1986], and then the two-stream adding method following equations (3)-(5) of *Chou* [1992] is applied to compute the upward and downward fluxes in both the clear and cloudy atmosphere.

Two column solar radiative-transfer models with UIUC89 and UIUC98 parameterizations of solar radiation were constructed to compare the solar heating rates. Three clear-sky atmospheric conditions chosen from the *McClatchey et al.* [1972] standard atmospheric profiles were tested with only
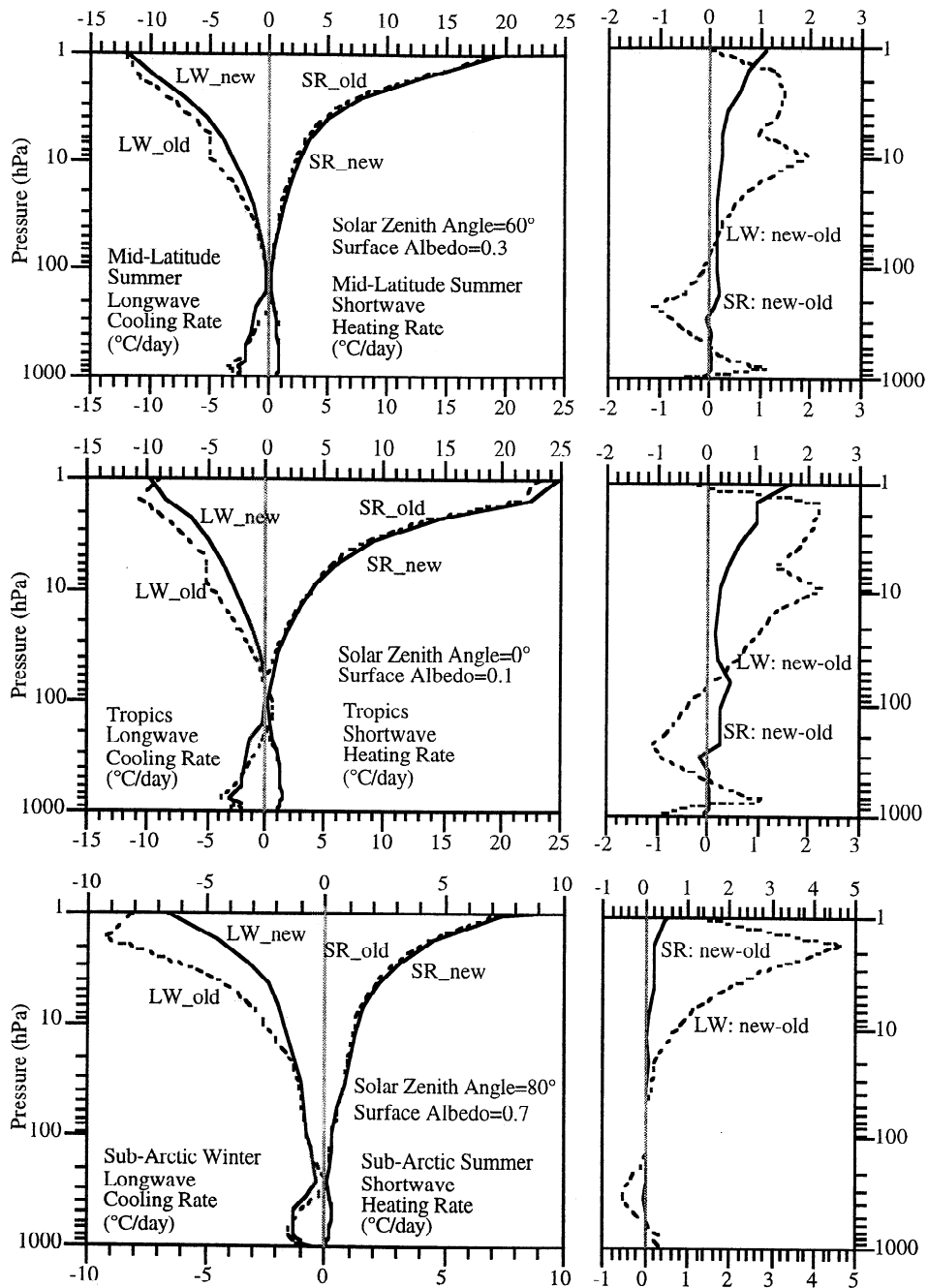
Figure 3. Longwave cooling and solar heating rates (°C d^{-1}) calculated using two 24-layer column radiative-transfer models, one using the UIUC98 radiation routines of the UIUC 24-L ST-GCM (labeled as "new") and the other using the UIUC89 radiation routines [Oh, 1989] of the UIUC 7-L and 11-L AGCMs (labeled as "old"). Four standard clear-sky atmospheric profiles of McClatchey et al. [1972] are considered: (top) midlatitude summer, (middle) tropics, and (bottom) the subarctic winter for longwave radiation and subarctic summer for solar radiation. The difference between the longwave cooling rates and the difference between the solar heating rates of the "new" and "old" radiation routines are presented on the right for each atmospheric condition. In all plots, only CO_2, H_2O, and O_3 are included in the radiative-transfer calculation.

the major absorbers of solar radiation (H_2O, O_3, and CO_2) included: (1) the midlatitude summer, with a solar zenith angle of 60° and surface albedo of 0.3, (2) the tropics, with a solar zenith angle of 0° and surface albedo of 0.1, and (3) the subarctic summer, with a zenith angle of 80° and surface albedo of 0.7. The calculated heating rates using the UIUC98 and

UIUC89 solar radiation schemes and their differences are shown in Figure 3, separately for the three atmospheric conditions. These two schemes result in nearly identical heating rates in the troposphere. In the stratosphere, the heating rate by the UIUC89 scheme is generally smaller than that by the UIUC98 scheme, and the discrepancy increases with height.

Table 2. Optical Properties of Sulfate Aerosol (75% H_2SO_4 and 25% H_2O) Computed From a Mie Theory Model and Integrated Over the 11 Spectral Bands of the Solar Radiation Model

Solar Band	Spectral Range, μm	Specific Extinction, $m^2 g^{-1}$	Single Scattering Albedo	Asymmetry Factor
1	0.175 - 0.225	9.266970	1.000000	0.681185
2	0.225 - 0.245	9.598478	1.000000	0.689153
	0.260 - 0.280	9.752305	1.000000	0.702173
3	0.245 - 0.260	9.700645	1.000000	0.695448
4	0.280 - 0.295	9.755453	1.000000	0.708951
5	0.295 - 0.310	9.715019	1.000000	0.714398
6	0.310 - 0.320	9.653944	1.000000	0.718529
7	0.320 - 0.400	9.205408	1.000000	0.730148
8	0.400 - 0.700	6.556963	1.000000	0.724810
9	0.700 - 1.22	2.608097	0.999987	0.627487
10	1.22 - 2.27	0.555460	0.985749	0.407517
11	2.27 - 10.0	0.383464	0.144101	0.091496

The maximum differences occur near the model top and are 1.1°C d^{-1} for the midlatitude summer, 1.5°C d^{-1} for the tropics, and 0.4°C d^{-1} for the subarctic summer.

2.2.4. Aerosol. In the ST-GCM the radiative effects of aerosols on terrestrial and/or solar radiation can be turned on in the troposphere and/or stratosphere, depending on the research interest. Both scattering and absorption are included in the solar radiation parameterization, while absorption and emission are included in the terrestrial radiation parameterization. In the present version of the 24-L ST-GCM, the radiative properties (specific extinction, single-scattering albedo, and asymmetry factor) of tropospheric sulfate aerosol have been calculated off-line by our Mie scattering model [*Boucher et al.*, 1998]. We assume that (1) aerosol particles consist of 75% sulfuric acid and 25% water, (2) the fraction of fine-particle mass that is sulfate is 60% [*Kiehl and Briegleb*, 1993], and (3) the aerosol size distribution follows a modified Gamma function [*World Meteorological Organization (WMO)*, 1986]. The complex index of refraction as a function of wavelength follows the WMO [1986] report.

The Mie scattering model was run with a high spectral resolution of 0.005 μm to compute the specific extinction, single-scattering albedo, and asymmetry factor. These optical properties in high spectral resolution were then integrated to the 11 broadbands of the solar radiation model and the nine broadbands of the terrestrial radiation model. Table 2 presents the solar spectral bands, together with the calculated specific extinction, single-scattering albedo, and asymmetry factor for sulfate aerosol in each band. The single-scattering albedo for sulfate aerosol is set to be 0 for all bands of terrestrial radiation since scattering does not occur there. The spectral extinction efficiency of terrestrial radiation by sulfate aerosol in each band is not shown here. This aerosol model has also been installed in our 11-layer troposphere/lower-stratosphere GCM [*Wang*, 1996; *Schlesinger et al.*, 1997a; *Wang and Schlesinger*, 1999], with appropriate modifications, and used

to study global and regional climate changes induced by the direct solar radiative forcing of anthropogenic sulfate aerosol [*Schlesinger et al.*, 1997b]. Simulation results from the 11-layer troposphere/lower-stratosphere GCM are available at ftp://crga.atmos.uiuc.edu/pub/emf/ for scientists to study the impacts of global and regional sulfate aerosol emissions.

2.2.5. Gravity wave drag. Gravity waves excited when stably stratified air flows over irregular terrain are able to transport horizontal momentum vertically. Parameterization of the drag effect of orographic gravity waves with spatial scales smaller than those resolved by an AGCM's grid is important. Usually, unrealistically intense midlatitude eastward surface winds exist in GCMs without parameterization of orographic gravity wave drag [*Hamilton*, 1996]. Other processes, such as moist convection, the development of dynamical instabilities of the Kelvin-Helmholtz type, geostrophic adjustment, and frontal zones, can also produce gravity waves and transfer mean momentum between the troposphere and the stratosphere/mesosphere. Nonorographic gravity waves generally have nonzero phase speeds and are less well understood at present than orographically excited gravity waves.

In the past two decades, considerable effort has been made to understand and parameterize gravity wave drag (GWD), with more attention paid to nonorographic gravity wave drag in recent years. A few different parameterization schemes of orographically excited gravity wave drag have been widely used in both numerical weather prediction models and general circulation models. Stimulated by *Lindzen*'s [1981] work on the simple parameterization of wave breaking associated with the onset of convective instability, *McFarlane* [1987] designed a wave drag parameterization based on linear theory for steady monochromatic waves, with the momentum flux divergence being represented by the wave-saturation assumption, and applied it to the Canadian Climate Center T21 spectral climate model. *Palmer et al.* [1986] independently developed and tested another orographic wave drag parameterization,

also based on Lindzen's wave-saturation hypothesis, in the United Kingdom Meteorological Office gridded general circulation model.

We have included *Palmer et al.*'s [1986] parameterization of orographically excited gravity wave drag in the 24-L ST-GCM. In this parameterization the surface stress is proportional to the near-surface wind speed and static stability and to the variance of the subgrid-scale orography, and wave breaking depends on the Richardson number. The vertical profile of wind stress is determined by a saturation hypothesis, whereby breaking waves are maintained at marginal stability. To use the scheme in the 24-L ST-GCM, a modification has been made to allow 90% of the horizontal momentum transported by gravity waves to exit the model top if the wave-breaking level does not occur within the model. This scheme requires tuning of several parameters to obtain the best wave-breaking effect, for example, the subgrid-scale mountain wavenumber and the upper limit of the subgrid-scale mountain-height variance.

To determine the effect of the parameterized orographic GWD on the 24-L ST-GCM's performance, two 180-day perpetual January simulations have been performed, one with the GWD parameterization and one without. The first 60 days of each simulation are taken as spin-up time, and the last 120 days of each simulation are used for comparison. Figure 4 shows the sea level pressure averaged over the last 120 days of the two simulations, together with the observed January sea level pressure climatology derived from the NCEP/NCAR reanalysis averaged from 1979 through 1995, which is provided on the Internet by the Climate Diagnostics Center, U.S. Department of Commerce, NOAA (available at http://www.cdc.noaa.gov/cdc/data.nmc.reanalysis.html). Distinguishable differences exist in the Northern Hemisphere between the simulated sea level pressure fields with and without GWD. With GWD, the Icelandic and Aleutian lows and the Siberian and North American highs are well simulated compared to the observations, though the subtropical high in the Pacific is still ~ 10 hPa stronger than observed. The overly intense surface westerly winds in the Northern Hemisphere middle latitudes in the simulation without GWD are greatly reduced by the orographic GWD parameterization.

Figure 5 shows the zonal-mean zonal wind and temperature averaged over the last 120 days of the two simulations, together with observation for January. The observed wind and temperature below 10 hPa are derived from the NCEP/NCAR Reanalysis averaged from 1979 through 1995, and above 10 hPa from the COSPAR International Reference Atmosphere 1986 (CIRA-86) [*Rees et al.*, 1990], which is maintained by the British National Space Science Data Center. The CIRA-86 data cover latitudes only from 80°S to 80°N. With GWD the simulated positions and magnitudes of tropospheric westerly centers are close to the observation data, especially in the Northern Hemisphere. The influence of the GWD parameterization on the Southern Hemisphere circulation is negligible. Unfortunately, the simulated polar-night jet in the northern lower stratosphere at about 10 hPa is too weak and is shifted equatorward of its observed position. The simulated zonal-mean temperature in the northern polar stratosphere between 100 and 10 hPa is ~ 10°C warmer than observed with the GWD parameterization and ~ 15°C colder than observed without the GWD parameterization. We have compared Figure 5 with pictures drawn using data averaged over the last 60 or 90 days of the 180-day simulation and obtained

qualitatively the same results, though the magnitudes of the temperature and wind anomalies change slightly.

Palmer et al. [1986] performed two perpetual January simulations using the U. K. Meteorological Office 11-layer GCM with and without the GWD parameterization included. They found a temperature difference of about +20°C near the tropopause in the Northern Hemisphere and a zonal-mean zonal wind decrease of ~20 m s^{-1} near the top of the model centered in the midlatitudes. All information indicates that our 24-L ST-GCM might have suffered excessive wind deceleration in the northern lower stratosphere, which in turn causes excessive warming in the northern polar stratosphere.

On the basis of this conjecture, we have conducted a set of perpetual January simulations by changing the tunable parameters within the orographic GWD scheme and/or by applying the orographic GWD parameterization for the troposphere or the troposphere and lower stratosphere alone. We changed the upper limit for the variance of the subgrid-scale orography (denoted as H) from 200 to 1000 m, and the representative horizontal wavenumber of the subgrid-scale orography from 1.0×10^{-4} to 0.6×10^{-5} (denoted as K). Unfortunately, none of these simulations proved to be satisfactory. In one extreme, if H and/or K are too small ($H = 200$ m, $K = 0.6 \times 10^{-5}$), the GWD parameterization has no detectable effect. The simulated northern polar-night jet is too strong and not separated from the tropospheric subtropical jet, and the simulation of sea level pressure is not improved. In the other extreme, if H and/or K are too large ($H = 1000$ m, $K = 1.0 \times 10^{-4}$), the northern polar-night jet and the tropospheric subtropical jet are separated, but the northern polar-night jet becomes too weak, and its core in the lower stratosphere is shifted to the mid-latitudes, and a large warm bias occurs in the northern polar region. The best choice we found for the 24-L ST-GCM is to set $H = 700$ m and $K = 2.5 \times 10^{-5}$ and apply the GWD parameterization to the entire atmosphere, as used in the above perpetual January simulation.

Despite this shortcoming of this orographic-type GWD parameterization, we have decided to keep it presently in the UIUC 24-L ST-GCM for three reasons. First, it does greatly improve the simulation in the troposphere and near the surface. Second, how to parameterize tropospheric/lower stratospheric subgrid-scale GWD in GCMs is still not settled. It is even less clear than how to parameterize subgrid-scale GWD in the mesosphere. Some basic questions remain to be solved [*World Climate Research Project*, 1998]. Third, some improved GWD parameterization schemes incorporating anisotropic orography and considering spectral property and different sources of subgrid-scale gravity waves have been developed recently [e.g., *Medvedev and Klaassen*, 1995; *Hines*, 1997a, b; *Alexander and Dunkerton*, 1999; *Gregory et al.*, 1998; *Medvedev et al.*, 1998]. For example, the scheme developed by *Alexander and Dunkerton* [1999] can be applied in principle to subgrid-scale gravity waves in GCMs generated by mountains, tropical convection, and wind shear. We look forward to evaluating these newly developed GWD parameterizations in the future.

3. Simulation of the Present Climate

Here we present results from a 15-year control simulation of the model. For this simulation the distributions of sea-surface temperature and sea ice were prescribed from the AMIP-II monthly mean distributions, which are the averages from 1979
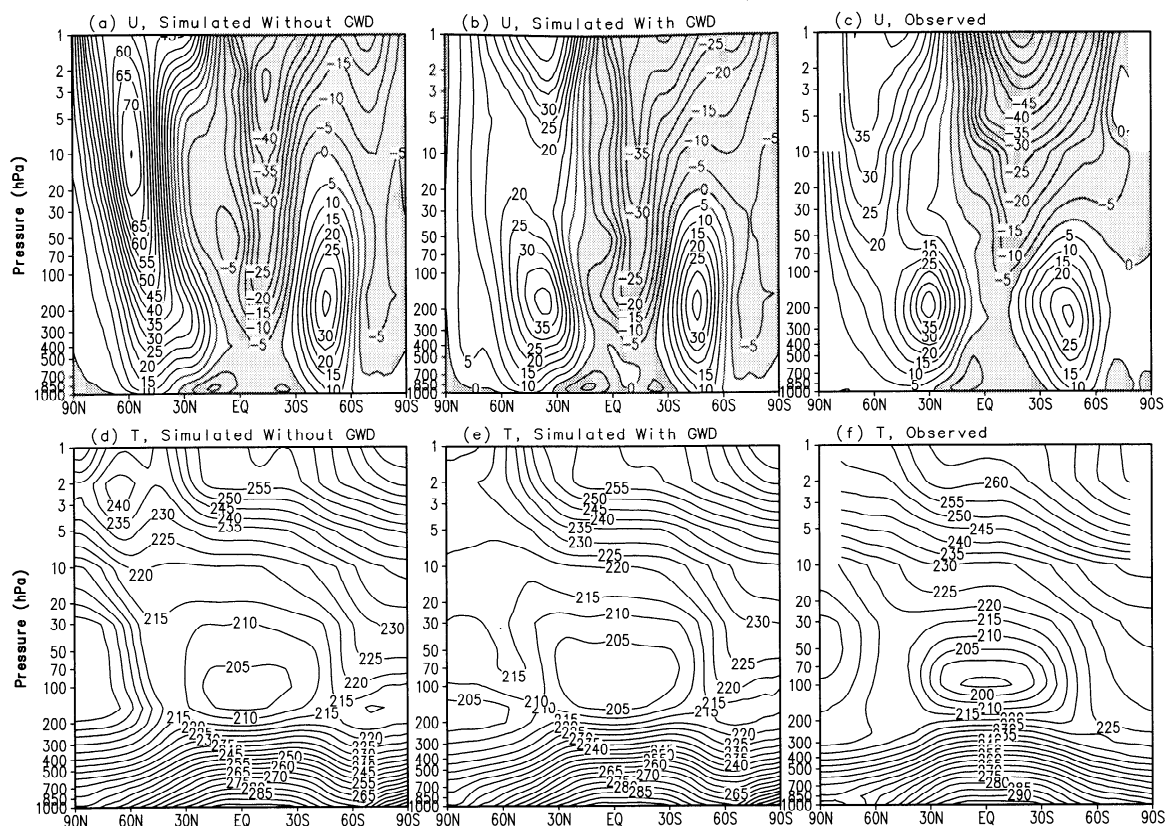
Figure 4. Comparison of sea level pressure fields between two perpetual January simulations (a) without and (b) with orographic GWD parameterization. In each 180-day simulation the data from the last 120 days were saved to derive the mean sea level pressure. (c) The observed values are from the NCEP/NCAR Reanalysis averaged from 1979 through 1995. The contour interval is 5 hPa. Pressure values less than 1010 hPa are shaded.

through 1996 [*Gleckler*, 1999], and were updated daily by interpolation between consecutive monthly mean values. The three-dimensional ozone data [*Wang et al.*, 1995] recommended by the AMIP-II panel were used. Tropospheric natural sulfate aerosol from *Langner and Rohde*'s [1991] slow-oxidation simulation was included in the model as tropospheric background aerosol, and only its direct radiative effect, scattering and absorption of solar radiation and absorption of longwave radiation, was included. The effective radius of water cloud droplets was taken to be 12 μm rather than relating it to the aerosol concentration as described in section

2.2.3. Therefore neither the direct nor the indirect radiative forcing of anthropogenic sulfate aerosol was included in this simulation since their uncertainties are still large, especially the indirect part [*Houghton et al.*, 1996].

If not indicated specifically, model results presented below are averages over the last 12 years of simulation. Simulated quantities are compared with available observations. Section 3.1 presents surface-air temperature, precipitation, cloud cover, and cloud radiative forcing. Section 3.2 examines zonal-mean atmospheric temperature and circulation, polar vortex, sudden stratospheric warming, the quasi-biennial os-

Figure 5. As in Figure 4, except for (a-c) zonal-mean zonal wind and (d-f) temperature. The contour interval is 5 m s^{-1} for wind and 5 K for temperature. Easterly winds are shaded. The observed wind and temperature below 10 hPa are from the NCEP/NCAR Reanalysis averaged from 1979 through 1995 and above 10 hPa from the COSPAR International Reference Atmosphere 1986 (CIRA-86) [*Rees et al.*, 1990].

cillation (QBO), and the equatorial semi-annual oscillation. Section 3.3 illustrates the Transformed-Eulerian-Mean circulation and eddy forcing of zonal-mean zonal wind. Throughout the paper we use DJF, MAM, JJA and SON to represent the seasons of December-January-February, March-April-May, June-July-August, and September-October-November, respectively.

3.1. Surface Quantities, Clouds, and Radiative Fluxes

3.1.1. Surface-air temperature. In the model, surface-air temperature is obtained by extrapolating the air temperature at the lowest model level, which is ~ 80 m above the ground in global average, downward to the surface with a lapse rate of 6.5°C km^{-1}. Presented in Figure 6a, 6c and 6e are the simulated annual mean surface-air temperature, the standard deviation of monthly mean surface-air temperature, which measures the variation of surface-air temperature within a year, and the march of zonal-mean monthly mean temperature from January to December. For a better view of the seasonal cycle, the temporal march is repeated for 2 years. Corresponding observations derived from the NCEP/NCAR Reanalysis averaged from 1979 through 1995 are presented in Figure 6b, 6d and 6f. The model simulates well the annual-mean surface-air temperature over land, except over Antarctica and Greenland, where the simulated temperature is ~ 3°-6°C warmer than observed. This bias is mainly caused by the smoothed model topography used. Over the ocean, the bias is generally less than 1°C

except over the Arctic. The figures of standard deviation and temporal march show that the model describes well the magnitude and phase of the variation of monthly mean surface-air temperature over the globe, except over Antarctica where the simulated standard deviation is much smaller than observed.

3.1.2. Precipitation. Daily precipitation rates (mm d^{-1}) are presented in Figure 7 in the same format as in Figure 6. The observations are averages from 1979 through 1996 [*Xie and Arkin*, 1997]. The model does capture the relative dry condition over northern Africa, western Australia, southern Africa, the two polar regions, and the west coast of the American continents and the relative wet condition over the tropics and southeastern Asia. The observed large precipitation rates over the warm pool and the Caribbean Sea associated with penetrative convection are simulated. The seasonal variation of tropical heavy precipitation associated with the north-south shift of the Intertropical Convergence Zone (ITCZ) is also captured. However, the model slightly overestimated precipitation over the western tropical Pacific and underestimated over the eastern tropical Pacific. The model also overestimates precipitation over the Eurasian and North American continents in DJF and MAM (not shown).

3.1.3. Cloud cover. The simulated and observed monthly mean cloud cover (%) is presented in Figure 8 in the same format as in Figure 6. The observed cloud cover is derived from the International Satellite Climate Climatology Project (ISCCP) data [*Rossow et al.*, 1991]. The model simulates well the annual-mean cloud cover and the march of zonal-mean cloud cover in time in the Northern Hemisphere and north of
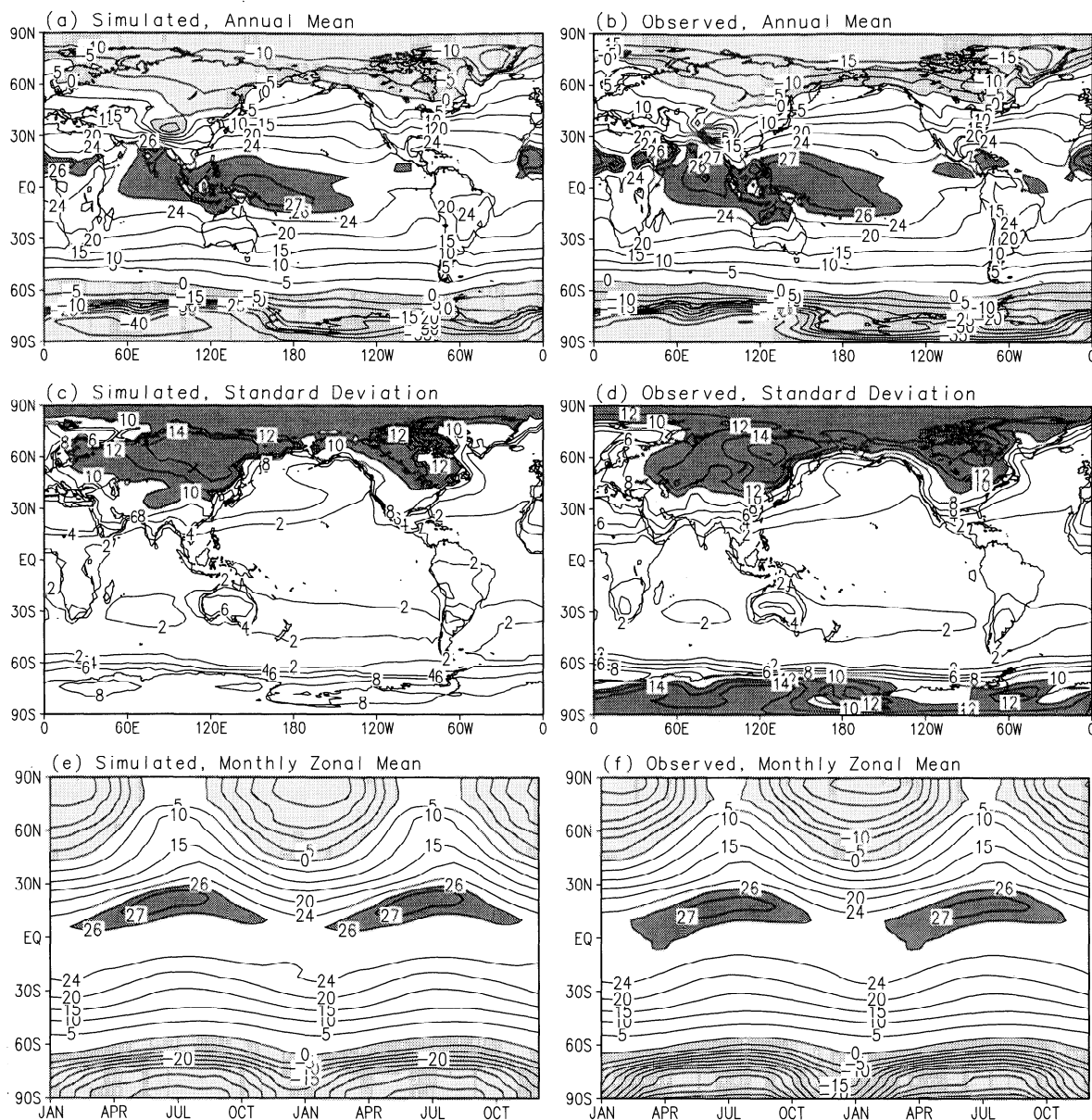
Figure 6. Simulated and observed (a, b) annual-mean surface-air temperature, (c, d) standard deviations of monthly mean surface-air temperature, (e, f) and the temporal march of monthly mean zonal-mean temperature. For a better view of the seasonal cycle, the temporal march is repeated for 2 years. In Figures 6a, 6b, 6e, and 6f the contour interval is 5°C with 24°C, 26°C, and 27°C contours added; temperatures higher than 26°C are heavily shaded, and temperatures below 0°C are lightly shaded. In Figures 6c and 6d, the contour interval is 2°C; standard deviations larger than 10°C are shaded. The observed temperatures are from the NCEP/NCAR Reanalysis averaged from 1979 through 1995.

50°S in the Southern Hemisphere. Similar to the observations, there are generally more clouds simulated over the oceans than over the continents and over warm oceanic regions than over cold oceanic regions. The simulated minimal cloud cover over the Sahara, western Australia and the eastern Pacific along the Chilean and Peruvian coasts, and the maximal cloud cover over the warm pool and Amazon are in good agreement with the observations. The model slightly underestimated the cloud cover over the North Pacific and North Atlantic and overestimated the cloud cover over northern Eurasia. Zonally averaged, the simulated cloud cover is ~ 5% larger than observed in the northern middle latitudes in all

seasons except DJF. Large errors exist in the high latitudes of the Southern Hemisphere. The model underestimated cloud cover by 20-30% along the coast of Antarctica.

We found that the scheme used in the model to diagnose the large-scale fractional cloud, which is based on *Sundqvist* [1978, 1988], is very sensitive to relative humidity. In high latitudes and near the poles, clouds are formed mainly through large-scale condensation. As described in section 2.2.2, large-scale fractional cloud is $b = 1-[(U_s-U) / (U_s-U_{00})]^{1/2}$, where U_s is the saturated relative humidity within the cloud, U is the actual relative humidity in the grid cell, and U_{00} is the relative humidity at which condensation can begin. If

$U < U_{00}$, $b = 0$. When we first tuned the model, we set U_s to be 100% and had to set U_{00} as large as 99% to obtain a simulated global-mean cloudiness of ~ 60%. In this case, it is difficult to form large-scale clouds in high latitudes and near the poles because there U is usually less than $U_{00} = 99\%$. Consequently, clouds are mostly convective clouds, although some stratiform clouds do form in the tropics and the subtropical lower troposphere. If we increase U_s, b will be smaller for any given U and U_{00}. Then the global-mean cloudiness becomes smaller. To compensate for this we can decrease U_{00} to increase b in order to keep the global-mean cloudiness unchanged. This decreased U_{00} allows some large-scale clouds to form in high latitudes and near the poles since the condition $U > U_{00}$ is more easily satisfied for a smaller U_{00}.

It turns out that b is very sensitive to U_s. Figure 9 shows the variations of b versus U for three cases: case A, $U_s = 100\%$ and $U_{00} = 99\%$; case B, $U_s = 100.5\%$ and $U_{00} = 99\%$; and case C, $U_s = 100.5\%$ and $U_{00} = 98\%$. The difference of b between case A and case B increases quickly as U increases, and reaches 58% at $U=100\%$. In the current version of the 24-L ST-GCM, $U_s = 100.6\%$ and $U_{00} = 98\%$ were used. This change did improve the simulation of cloud amount in high latitudes and near the poles compared to what we obtained with $U_s = 100\%$ and $U_{00} = 99\%$.

3.1.4. Cloud radiative forcing. We define the net radiative flux as $N = S - R$, where S is the net incoming solar flux, defined as positive downward, and R is the outgoing terrestrial flux, defined as positive upward. Cloud radiative forcing is
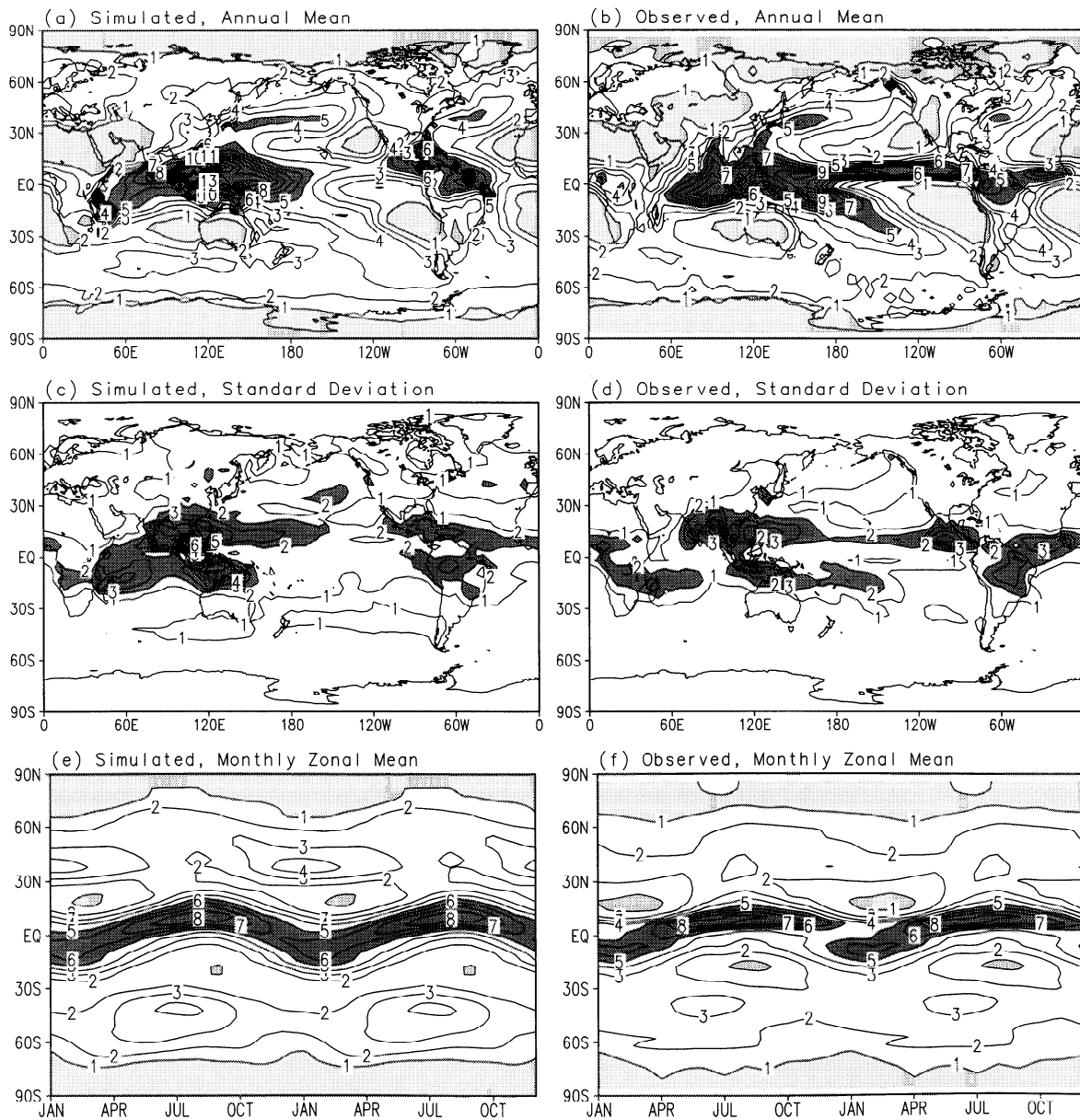
Figure 7. As in Figure 6, except for precipitation rate (mm d^{-1}). In Figures 7a, 7b, 7e, and 7f, precipitation rates larger than 5 mm d^{-1} are heavily shaded, and precipitation rates smaller than 1 mm d^{-1} are lightly shaded. In Figures 7c and 7d, standard deviations larger than 2 mm d^{-1} are shaded. The contour interval is 1 mm d^{-1} for all parts. The observed are averages from 1979 through 1996 [*Xie and Arkin*, 1997].
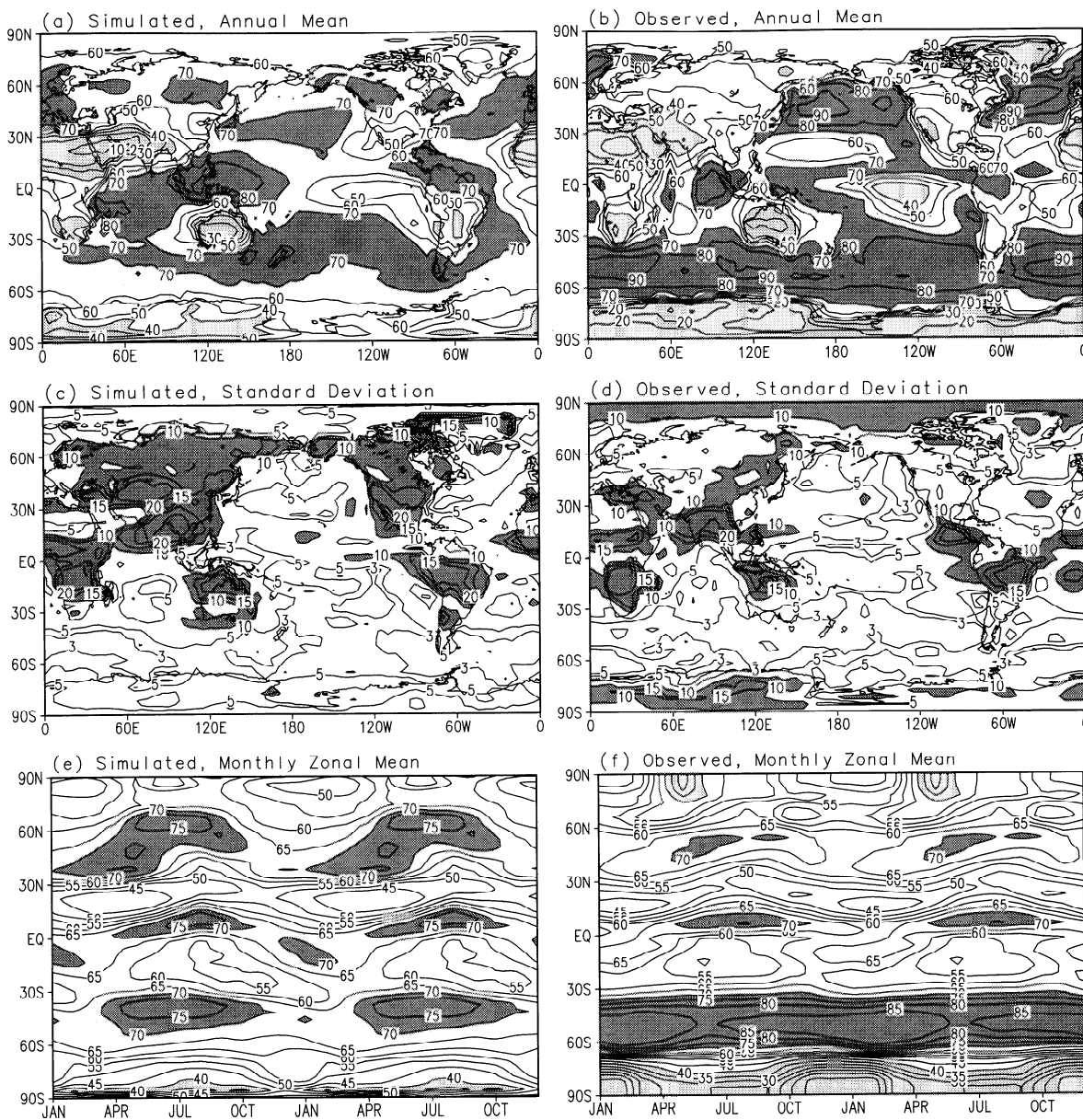
Figure 8. As in Figure 6, except for cloud cover (%). The contour interval is 10% in Figures 8a and 8b, and 5% in Figures 8e and 8f. In Figures 8c and 8d, contours are 1, 3, 5, 10, 15, 20, and 30%. In Figures 8a, 8b, 8e, and 8f, cloud cover larger than 70% is heavily shaded and cloud cover smaller than 40% is lightly shaded. In Figures 8c and 8d, standard deviations larger than 10% are shaded. The observed are ISCCP climatology [*Rossow et al.*, 1991].
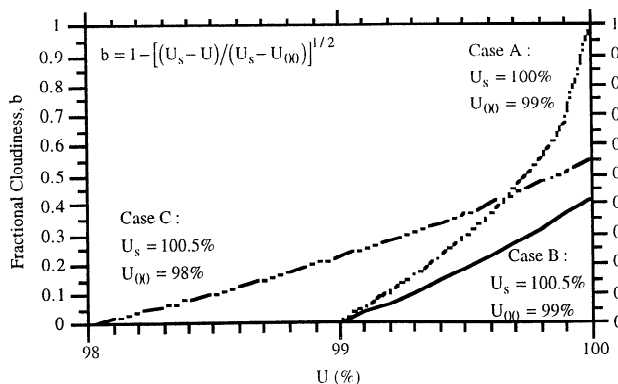

Figure 9. Variations of fractional cloudiness versus relative humidity for large-scale condensation.

given by $CRF = \Delta N = \Delta S - \Delta R$ at the top of the atmosphere (TOA), where Δ is the difference between the all-sky (cloudy sky) and clear-sky radiative fluxes. Positive (negative) CRF indicates that clouds radiatively heat (cool) the Earth-atmosphere system [*Cess et al.*, 1997]. CRF contains two components, the longwave (LW) CRF = $-\Delta R$, which is the difference of TOA outgoing longwave radiation (OLR) between cloudy sky and clear sky, and shortwave (SW) CRF = ΔS, which is the difference of TOA net incoming solar radiation between cloudy sky and clear sky. LW CRF is generally positive since clouds trap the outgoing longwave radiation in the atmosphere like greenhouse gases. SW CRF is generally negative since clouds reflect more incoming solar radiation back to space than they absorb. The LW CRF and SW CRF are pre-

sented in Figures 10 and 11, respectively, in the same format as in Figure 6. We derived the observed climatological CRF components from the Earth Radiation Budget Experiment (ERBE) measurements from 1985 through 1989, which were provided by the NASA Langley Research Center, Earth Observing System Data Information System (EOSDIS) Distributed Active Archive Center.

Over regions covered by clouds, the height of the cloud tops greatly influences the magnitude of the LW CRF [*Cess et al.*, 1997]. Generally, the model simulates well the geographical distribution and seasonal variation of the LW CRF, except between 40°S and 60°S, where the model does not simulate cloud cover well (Figure 8). The maximum LW CRF

in the tropics and its north-south shift from month to month along with the ITCZ are in good agreement with the observations.

When tuning the model, special attention was given to the simulation of the OLR over the warm-pool region, where a regional minimum OLR occurs over the high-SST surface because of the low emission temperature at the top of convective clouds. *Wang and Schlesinger* [1995, 1999] found that in order to correctly simulate the tropical intraseasonal oscillation using the UIUC 11-layer AGCM with any of the three convection schemes (the UIUC GCM's cumulus-convection scheme that includes a modified *Arakawa and Schubert* [1974] penetrative convection scheme and a mid-level convec-
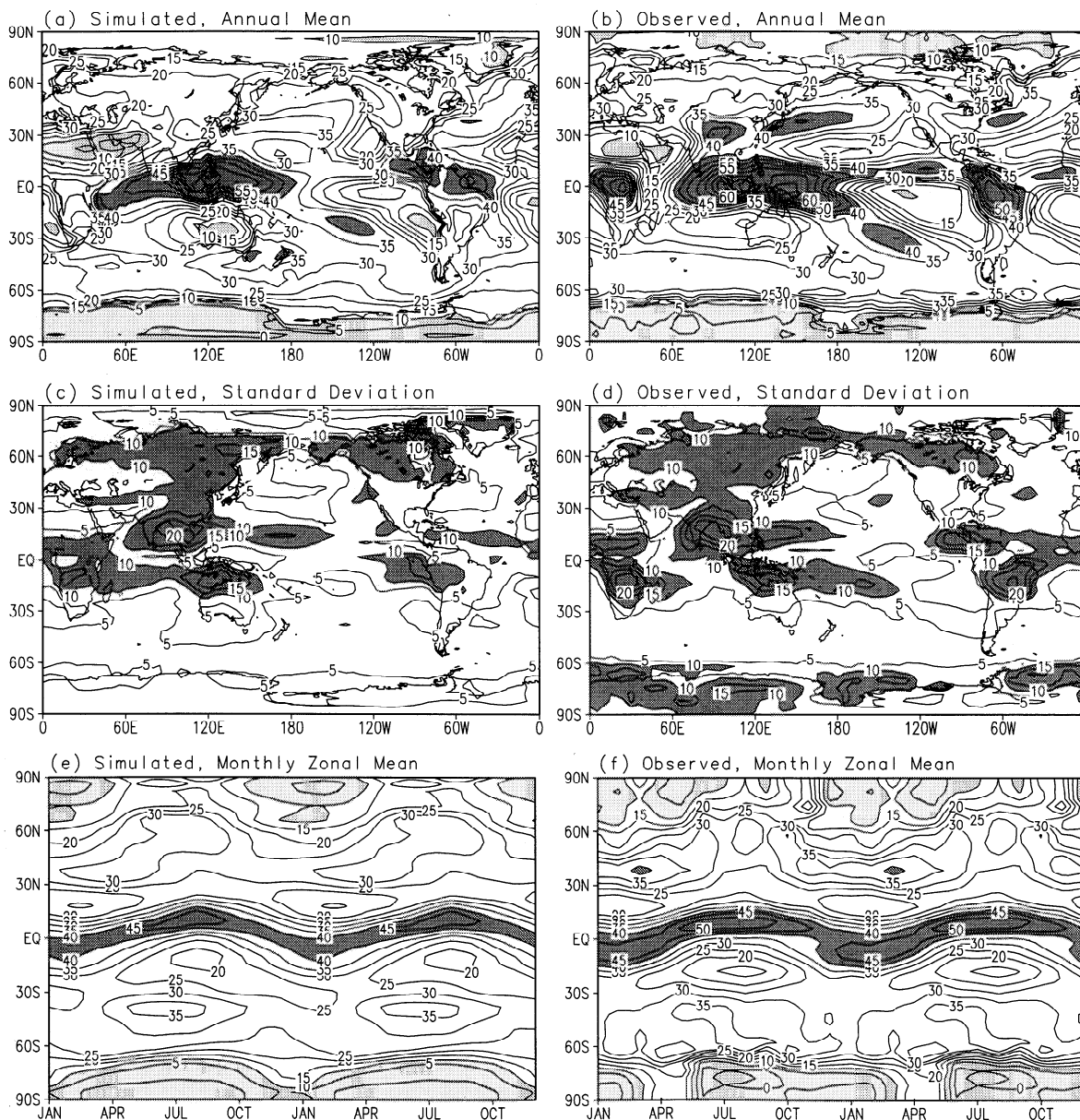
Figure 10. As in Figure 6, except for all-sky longwave cloud radiative forcing (LW CRF, W m^{-2}). In Figures 10a, 10b, 10e, and 10f, forcing values larger than 40 W m^{-2} are heavily shaded and smaller than 10 W m^{-2} are lightly shaded. In Figures 10c and 10d, standard deviations larger than 10 W m^{-2} are shaded. The contour interval is 5 W m^{-2} for all parts. The observations are the averages of the ERBE satellite data from 1985 through 1989.
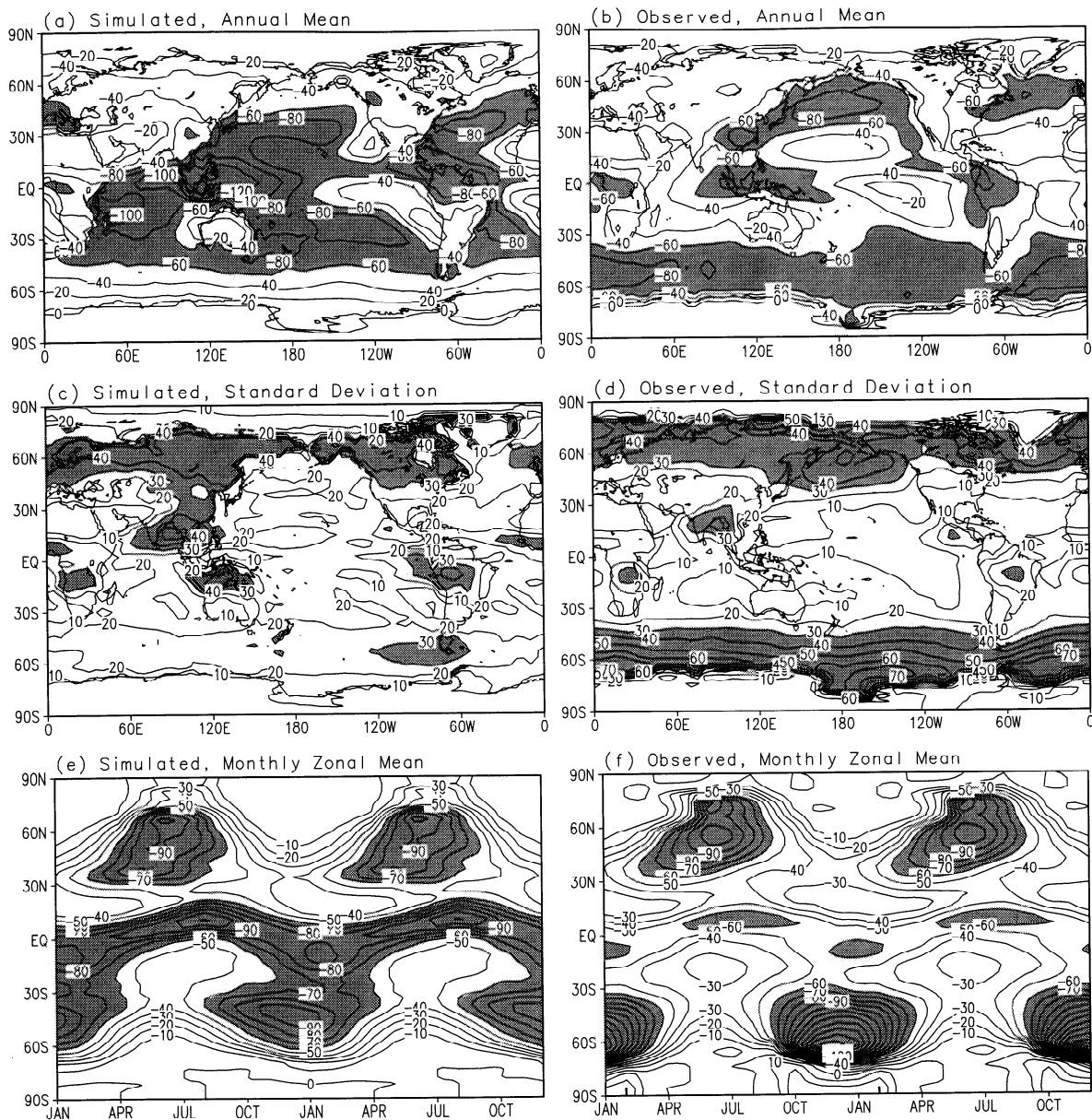
Figure 11. As in Figure 10, except for all-sky shortwave cloud radiative forcing (SW CRF, W m^{-2}). The contour interval is 20 W m^{-2} in Figures 11a and 11b, and 10 W m^{-2} in other panels. In Figures 11a, 11b, 11e, and 11f, forcing values smaller than -60 W m^{-2} are shaded. In Figures 11c and 11d, standard deviations larger than 30 W m^{-2} are shaded.

tion scheme [*Oh*, 1989], *Kuo*'s [1974] scheme, and *Manabe et al.*'s [1965] moist convective adjustment scheme) a large relative-humidity criterion, usually greater than 80%, must be applied as a threshold for the onset of convection. However, when this constraint was applied to the 24-L ST-GCM, the simulated penetrating convection in the tropics was too weak and the cloud tops were too low. This led to a 20 to 30 W m^{-2} higher-than-observed OLR in the warm-pool region and the resulting LW CRF was too small. It is found that for the 24-L ST-GCM a relative-humidity criterion of 50% best reproduces the observed LW CRF over the tropics. This criterion also yields a better simulation of the observed geographical distributions of precipitation and clouds, especially the distinct land-ocean contrast of cloud cover in the Northern Hemi-

sphere midlatitudes. The effect of this revised criterion on the 24-L ST-GCM's ability to simulate the tropical intraseasonal oscillation remains to be analyzed.

The model captures the basic geographical distribution and seasonal variation of the SW CRF (Figure 11). The model simulates the SW CRF better in the Northern Hemisphere than in the Southern Hemisphere and much better over the continents than over the oceans. Generally, the model overestimated the SW CRF in the tropics and subtropics but underestimated the SW CRF in high latitudes. The largest bias occurs near 60°S in January. This occurs because the model underestimates cloud cover by as much as 20-30% there. In addition to the simulated total cloud cover and the vertical distribution of cloudiness, the surface albedo also greatly influences

the distribution of SW CRF. Figure 12 shows the geographical distributions of the simulated clear-sky planetary albedo and their percentage differences from the ERBE observations in January and July. It can be seen that in both months the simulated clear-sky albedo is smaller than observed over open-water surface. The simulated global annual-mean clear-sky albedo is 11.2% smaller than observed. The source of the discrepancy may come from the schemes used to calculate the surface albedo over open water for direct and diffusive solar fluxes. In the model the surface albedo is fixed to be 0.07 for the diffusive solar flux and is a function of solar zenith angle for direct solar flux [Briegleb et al., 1986].

In this section we have compared the geographical distributions and seasonal variations of the simulated surface-air temperature, precipitation, cloud cover, and cloud radiative forcing with observations. In Table 3 we present their annual means over the globe and over the warm pool ($10°S$-$10°N$; $140°$-$170°E$). We also include in Table 3 the outgoing longwave radiation and net incoming solar radiation at the top of the atmosphere in all-sky and clear-sky conditions, which are used to derive the cloud radiative forcing. Generally, the simulated magnitudes of these quantities match the observed well over the globe and the warm-pool area. One exception is the all-sky TOA net incoming solar radiation over the warm pool. The simulated is 35 W m^{-2} smaller than the observed by ERBE. This large discrepancy can be explained in part by the overestimated cloud cover over the warm pool; Table 3 shows that the simulated cloud cover is 78% and the observed is

71.6%. Another possible explanation is that the model may have underestimated the absorption of solar radiation by clouds over the warm pool. Such an underestimate has been found in many other GCMs and been discussed widely [e.g., Cess et al., 1995; Ramanathan et al., 1995]. Over the warm pool, the simulated clear-sky TOA OLR matches the observed well, but the all-sky TOA OLR is 8 W m^{-2} larger than observed. This indicates that the cloud top of convective cloud in the warm-pool area may still not be high enough, even though a relative-humidity criterion of 50% has been used for the onset of convection. Another bias is the clear-sky TOA incoming shortwave radiation. The simulated value is a few W m^{-2} larger than observed for both the global mean and the warm-pool mean. This is probably because of the underestimate of the clear-sky planetary albedo by the model (Figure 12). It should be pointed out that when we developed the model we tried to simulate well both the global means of the above quantities and their geographical distributions. It can be seen from Table 3 that even though the simulated all-sky TOA net incoming solar radiation over the warm pool is much smaller than observed, the global-mean value matches the observed very well as a result of cancellation of errors over the globe. This is also true for other all-sky quantities. A similar cancellation of errors was also found by Wild et al. [1995] when they compared radiative fluxes simulated by three versions of ECHAM GCMs and a few other GCMs with observations. Wild et al. [1995] mainly focused on the surface radiative fluxes.
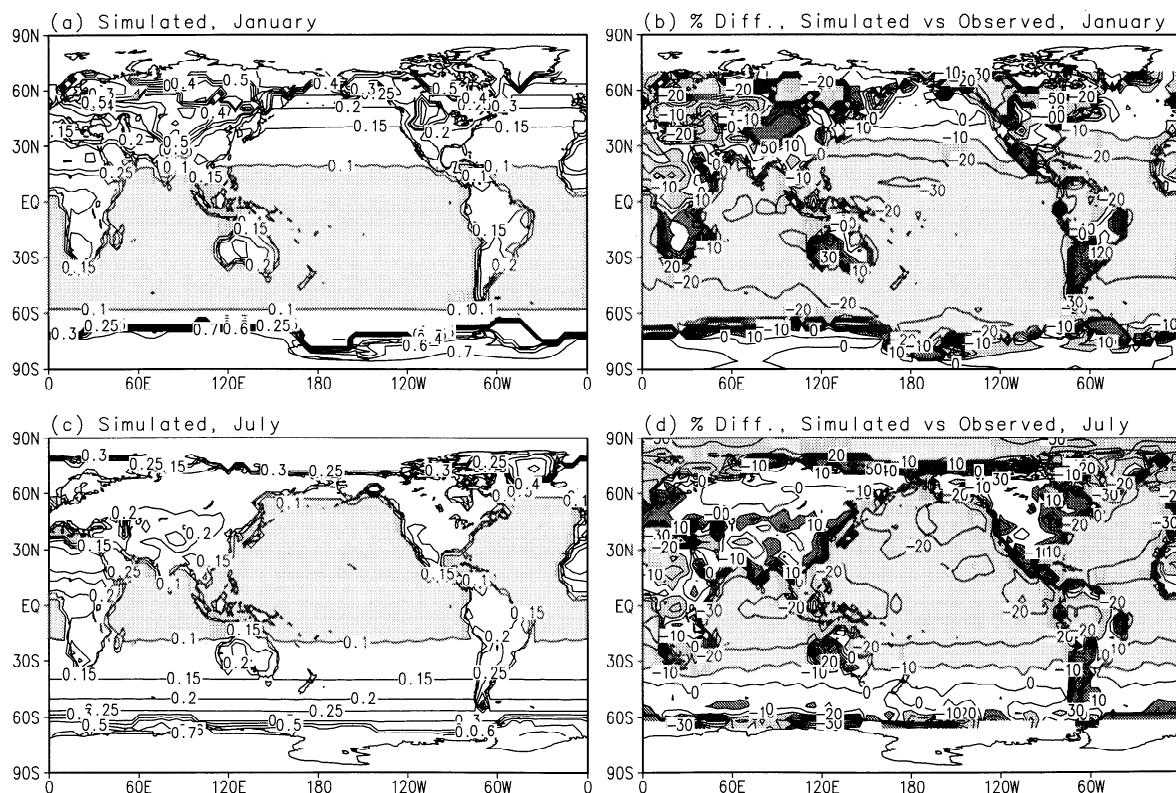

Figure 12. Simulated clear-sky planetary albedo in (a) January and (c) July, and their percentage differences from the ERBE satellite observations in (b) January and (d) July. In Figures 12a and 12c the contour interval is 0.05 for values smaller than 0.3 and 0.1 for those larger than 0.3; values smaller than 0.1 are shaded. In Figures 12b and 12d the contour interval is 10%; percentage differences larger than 10% are heavily shaded and smaller than -10% are lightly shaded.

Table 3. Global and Warm-Pool Averages of Selected Annual-Mean Quantities From Model Simulation and Observations

Quantity	Global Mean		Warm Pool (10°S-10°N; 140°E-170°E)	
	Simulation	Observation	Simulation	Observation
Surface-Air Temperature (°C)	13.9	14.2	26.7	27.4
Cloud Cover (%)	62.4	62.2	78.0	71.6
Precipitation, mm d^{-1}				
Large-Scale	1.28	-	1.85	-
Convective	1.68	-	6.69	-
Total	2.96	2.69	8.54	8.33
TOA OLR, W m^{-2}				
All-Sky	-237.6	-235.3	-236.0	-227.9
Clear Sky	-264.8	-264.6	-284.0	-285.7
LW CRF	27.2	29.3	48.0	57.8
TOA Net SW, W m^{-2}				
All-Sky	239.2	240.2	273.9	309.3
Clear-Sky	294.3	287.9	380.4	371.9
SW CRF	-55.1	-47.7	-106.5	-62.6

Source of observation: Surface-air temperature, NCEP/NCAR reanalysis, averages from 1979 through 1995; cloud cover, ISCCP climatology [*Rossow et al.*, 1991]; precipitation, *Xie and Arkin* [1997]; and TOA OLR and TOA Net SW, ERBE satellite observation, averages from 1985 through 1989.

3.2 Atmospheric Temperature and Zonal Wind

3.2.1. Zonal-mean temperature. Latitude-height cross sections of the simulated seasonal-mean zonal-mean temperature are presented in Figure 13 for the four seasons of the year, together with the corresponding observations and the differences between the simulated and the observed zonal-mean temperatures. Below 10 hPa the observed temperatures are the averages of the NCEP/NCAR Reanalysis from 1979 through 1995. Above 10 hPa the observed temperatures are from the Committee of Space Research (COSPAR) International Reference Atmosphere 1986 (CIRA-86) [*Rees et al.*, 1990].

In all four seasons the model simulates fairly well the temperatures in the troposphere and stratosphere everywhere except in the polar stratosphere. Temperature differences are less than 5°C in the troposphere and less than 10°C in the stratosphere in middle and low latitudes. The locations of the tropical tropopause and midlatitude temperature gradients in the troposphere are well simulated. In the stratosphere, the model captures the opposite distributions of the pole-to-pole temperature gradient in JJA and DJF and the reversals of the temperature gradient in MAM and SON.

The model is generally colder than observed, except in the middle polar stratosphere during polar night and near the stratopause. *Swinbank et al.* [1998] found a similar systematic cold bias in the UKMO Unified Model. They attributed that bias primarily to an inaccurately simulated longwave cooling rate. The bias in the UIUC 24-L ST-GCM occurs for a different reason. The longwave radiation scheme of the 24-L ST-GCM can produce clear-sky cooling rates with errors less than 0.4°C d^{-1} from the Earth's surface up to 0.01 hPa when compared with line-by-line calculations [*Chou and Suarez*, 1994]. Table 3 shows that the simulated global-mean clear-sky TOA OLR and the simulated mean clear-sky TOA OLR over the warm pool match the ERBE satellite observations very well. The simulated clear-sky TOA net incoming solar

radiation also matches the ERBE satellite observation reasonably well. The cold bias in the 24-L ST-GCM is probably caused by an inaccurate radiative-transfer calculation in the cloudy atmosphere. Cloud distribution, cloud optical properties, and the assumed cloud overlap in the model influence the simulated radiative heating and cooling of the atmosphere by clouds. The model has a smaller LW CRF and a larger SW CRF than the ERBE satellite observations. In the tropics the simulated absorption of solar radiation by clouds is substantially smaller than observed, especially over the warm pool (Table 3). These errors lead to an overall larger-than-observed cooling effect by clouds. The cold bias in the troposphere in turn leads to a colder-than-observed lower and middle stratosphere because less longwave radiation is intercepted by the stratospheric atmosphere.

Near its top the model is 5–10°C warmer than observed because of a momentum damping [*Hansen et al.*, 1983] applied to the model's top layer, the "sponge layer." This sponge layer absorbs vertically propagating waves forced from below and allows a large time step to be used for the numerical integration of the model's dynamical processes which keeps the model from suffering linear computational instability.

In all seasons in the lower stratosphere the model is 10°–20°C colder than observed in the Northern Hemisphere and 15°–25°C colder in the Southern Hemisphere. These cold biases are common to many other GCMs. In SON and DJF the model is 5°–15°C warmer than observed in the middle and upper polar stratosphere in the Northern Hemisphere. In MAM and JJA the model is 5°–20°C warmer than observed in the upper polar stratosphere in the Southern Hemisphere. These warm biases do not exist in most other GCMs. Usually, systematic cold biases exist throughout the model atmosphere in the polar-night region, with a larger bias appearing in the upper stratosphere near 10 hPa [e.g., *Hamilton et al.*, 1995]. However, the Berlin Troposphere-Stratosphere-Mesosphere (TSM) GCM has a warm bias similar to that of the UIUC 24-L
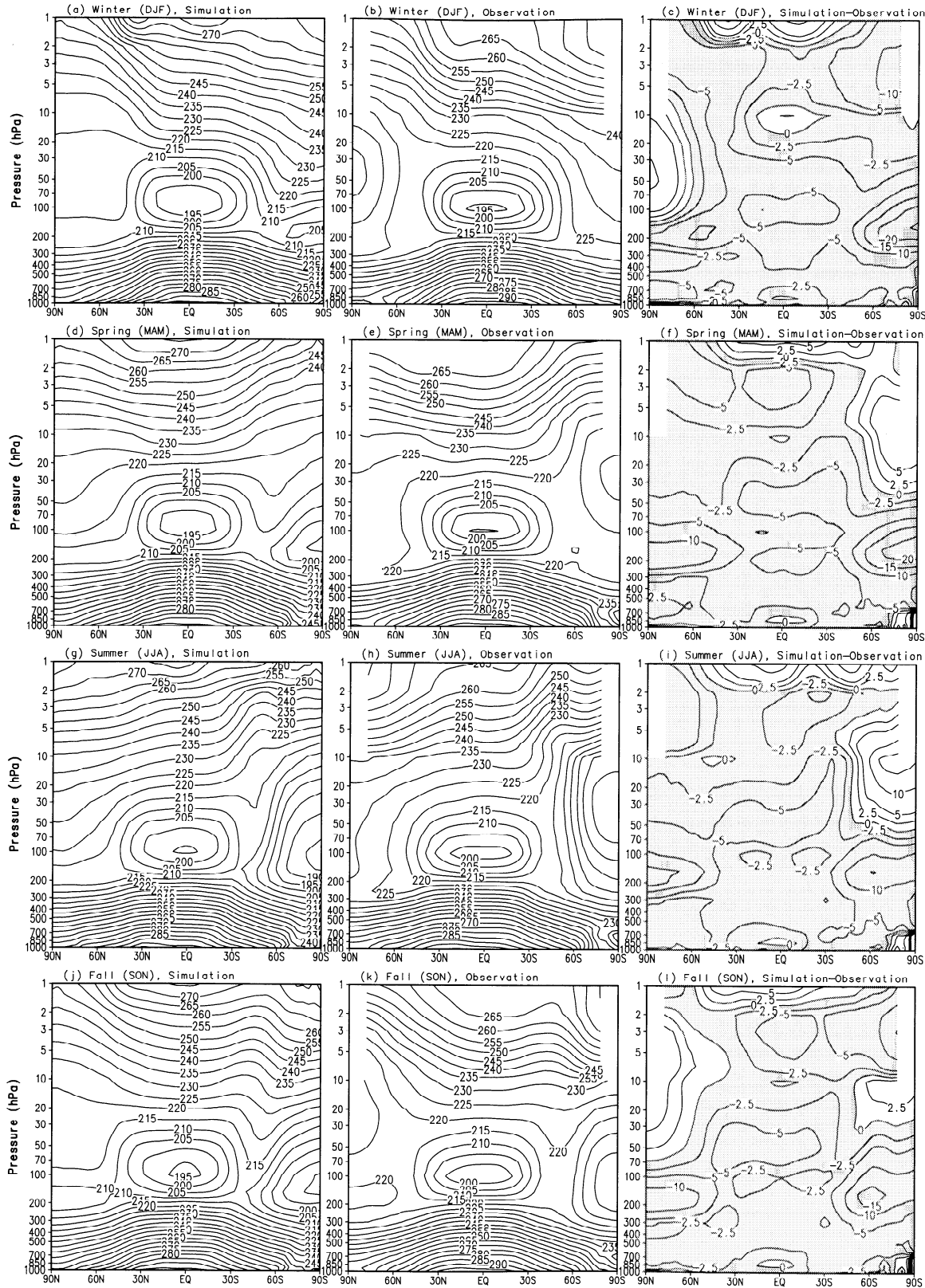
Figure 13. Latitude-altitude distributions of zonal-mean temperature (K) for winter (DJF), spring (MAM), summer (JJA) and fall (SON), simulated (left), observed (middle), and the differences between the simulated and observed (right). The contour interval is 5 K for all panels, with ±2.5 K contours added for the difference panels. Negative differences are shaded. The observed temperatures below 10 hPa are from the NCEP/NCAR Reanalysis, averaged from 1979 through 1995, and above 10 hPa from the COSPAR International Reference Atmosphere 1986 (CIRA-86) [*Rees et al.*, 1990].

ST-GCM in the polar stratospheres. *Langematz and Pawson* [1997] found that the warm bias in the Berlin TSM-GCM is primarily due to the inaccurately simulated radiative heating, which may result from a cooling-to-space approximation for longwave radiative transfer above 20 hPa. As shown by the sensitivity studies in section 2.2.5, the warm bias in the Northern Hemisphere in the UIUC ST-GCM is caused by the use of the *Palmer et al.* [1986] GWD parameterization. Without the parameterization, a cold bias prevails. The warm bias in the Southern Hemisphere is caused by the simulated larger-than-observed intensity of air-mass sinking in JJA [*Rozanov et al.*, 1999b].

3.2.2. Zonal-mean zonal wind. Latitude-height cross sections of the simulated seasonal-mean zonal-mean zonal wind are presented in Figure 14. In the troposphere, the model simulates well the locations and strengths of the subtropical jets in both hemispheres during all seasons, especially in the Northern Hemisphere. Similar to observations, the simulated Northern Hemisphere tropospheric jet is much stronger in DJF than in JJA. The differences between the simulated and the observed zonal-mean winds are generally less than 5 m s^{-1} in the troposphere. In the stratosphere in all seasons except DJF, the simulated westerly and easterly winds have approximately the observed strengths and positions. The transitions of westerly and easterly winds are captured. The tropospheric jets are well separated from the stratospheric polar-night jets in both boreal and austral winter. The simulation is better in the troposphere than in the stratosphere and in MAM and JJA than in SON and DJF. Uniquely, the 24-L ST-GCM simulates the observed equatorward tilt of the southern polar-night jet core in JJA. Most current other GCMs do not simulate the tilt of this jet well.

One deficiency of the model is that the simulated northern polar-night jet is too weak in the middle stratosphere, and the jet core is shifted equatorward of its observed position. The observed equatorward tilt of the northern polar-night jet core from the polar tropopause to the midlatitude stratopause is not properly simulated. The southern polar-night jet is also slightly weaker than observed. Most other GCMs simulate too strong polar-night jets. The reason is that the 24-L ST-GCM has warmer temperature in the middle-to-upper polar stratosphere than other GCMs, as discussed in section 3.2.1.

There are also some other discrepancies between the simulated and observed zonal winds. In DJF, the tropospheric subtropical jet in the Southern Hemisphere extends too high, up to 10 hPa, in contrast to the observed transition from westerly winds to easterly winds at ~ 50 hPa. This occurs via the thermal wind relation because the southern lower polar stratosphere is more than 20°C colder than observed in DJF. Near the tropical tropopause in MAM and SON, the simulated winds are westerly, but the observed winds are easterly. Also, the simulated strength of the stratospheric equatorial wind does not match the observed very well above 10 hPa.

3.2.3. Seasonal evolution of zonal wind at 10 hPa, 60°N and 60°S. The 24-L ST-GCM has been coupled in an off-line mode, and will be coupled interactively, with a chemistry-transport model [*Rozanov et al.*, 1999a, b] to simulate and understand the influence of interactive ozone photochemistry on greenhouse-gas-induced climate change, and the influence of greenhouse-gas-induced climate change on ozone, including the distribution of ultraviolet radiation at the Earth's surface. The transitions of stratospheric winds from

easterly to westerly and from westerly to easterly, and the break down of the polar vortices are important for the transport of trace gases and chemical processes within the polar regions. The simulated and observed variations of monthly mean zonal-mean zonal wind at 10 hPa, averaged over the last 12 model years of the simulation and from 1979 through 1995 for the observation, are presented in Figure 15. In the Northern Hemisphere the model simulates well the transitions from westerly to easterly in May and from easterly to westerly in September. However, the simulated westerly jet core is located at 30°N, which does not correspond to the observed position at 60°N. In the Southern Hemisphere the meridional extent, the strength, and seasonal variation of the polar vortex are well simulated. The strongest vortex appears in August and September. One shortcoming is that the simulated southern polar vortex does not break down in DJF; however, further examination shows that it does break down in 5 out of the 12 simulated years (not shown). This indicates that the simulated southern polar stratospheric wind has a rather large interannual variability. It is also noticed from Figure 15 that the simulated north-south shift of the maximum easterly wind and its strength in the tropics are reasonably realistic.

To further explore the annual cycle and interannual variability of the polar stratospheric vortices in both hemispheres, we present in Figure 16 the simulated and observed mean annual march of monthly mean zonal-mean zonal wind at 60°S and 60°N, respectively. The time axis runs from January to December at 60°S and from July to June at 60°N. At 60°S the simulated seasonal variation and strength of the zonal wind match the observed fairly well. In both the simulation and the observations the strongest westerly wind is established in the upper stratosphere in April and May and intensifies progressively at lower levels reaching its maximum near 10 hPa in August and September and further propagates downward to the lower stratosphere until November with a gradually weakening strength. The simulated strong vortex in the upper stratosphere in August and September is in good agreement with the observations. The local maximum near 10 hPa matches the observed, though a little weaker. Most other current middle-atmosphere GCMs tend to largely overestimate the vortex here [e.g., *Boville*, 1995; *Manzini and Bengtsson*, 1996; *Swinbank et al.*, 1998]. However, in the upper stratosphere the simulated westerly wind is established in February, one month earlier than observed, and breaks down in November, one month later than observed. It is also noticed that in the lower stratosphere in March and April, the simulated westerly wind is ~ 10 m s^{-1} larger than observed as a result of a colder-than-observed lower polar stratosphere.

At 60°N the model simulates the polar vortex poorly. The westerly wind decays too early in October and does not intensify and propagate further downward as does the observed. This deficiency is caused by the orographic GWD parameterization in the model as described in section 2.2.5.

3.2.4. Sudden stratospheric warming. The simulation of spontaneous sudden warmings in the polar stratosphere by a GCM is an important test of its capabilities. Many GCMs have succeeded in varying degrees in generating sudden stratospheric warmings, such as the UKMO Unified Model [*Swinbank et al.*, 1998], the Canadian MAM [*Beagley et al.*, 1997], and the ECHAM3.5 GCM [*Manzini and Bengtsson*, 1996]. We present in Figure 17 the variations of temperature at 10 hPa at the North Pole and South Pole during the last 3
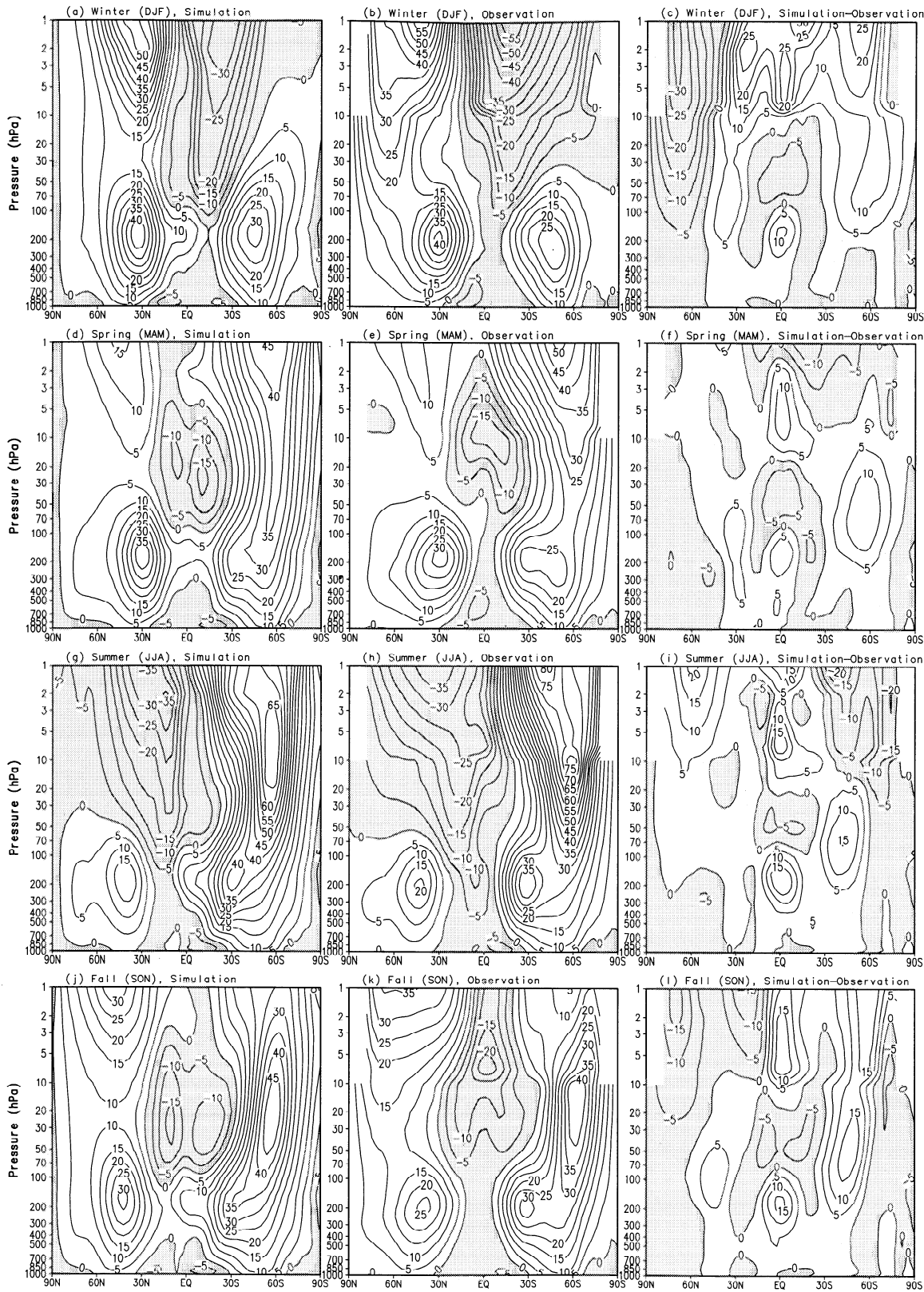
Figure 14. As in Figure 13, except for zonal-mean zonal wind (m s^{-1}). The contour interval is 5 m s^{-1} for all parts. Westerly winds and negative differences are shaded.

years of the simulation, sampled at 6-hour intervals. Each curve represents 1 simulated year. No sudden warmings exist at the South Pole, as in the real atmosphere. The model does show considerable variability at the North Pole from October

through March. Multiple sudden warmings occur at the North Pole. *Manzini and Bengtsson* [1996] showed that the observed North Pole sudden stratospheric warmings usually begin in January and end in April. Here the simulated
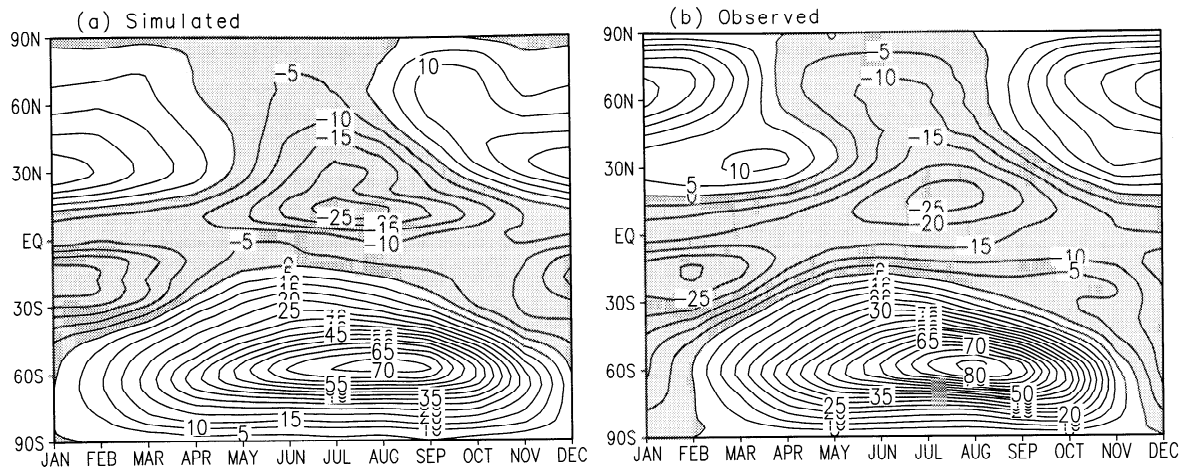
Figure 15. Annual march of zonal-mean zonal wind at 10 hPa from January to December for (a) the simulated model climatology and (b) the observed climatology. The contour interval is 5 m s^{-1}. Easterly winds are shaded.

warmings begin in October and end in March. The model presents a larger variability than the real atmosphere at the North Pole from October to December. Such overestimated early-winter variability has also been found in other GCMs,

namely, the UKMO Unified Model [*Swinbank et al.*, 1998] and the Canadian MAM [*Beagley et al.*, 1997]. To further illustrate the relation between the simulated sudden warmings and the zonal wind near the poles, we present in Figure 18
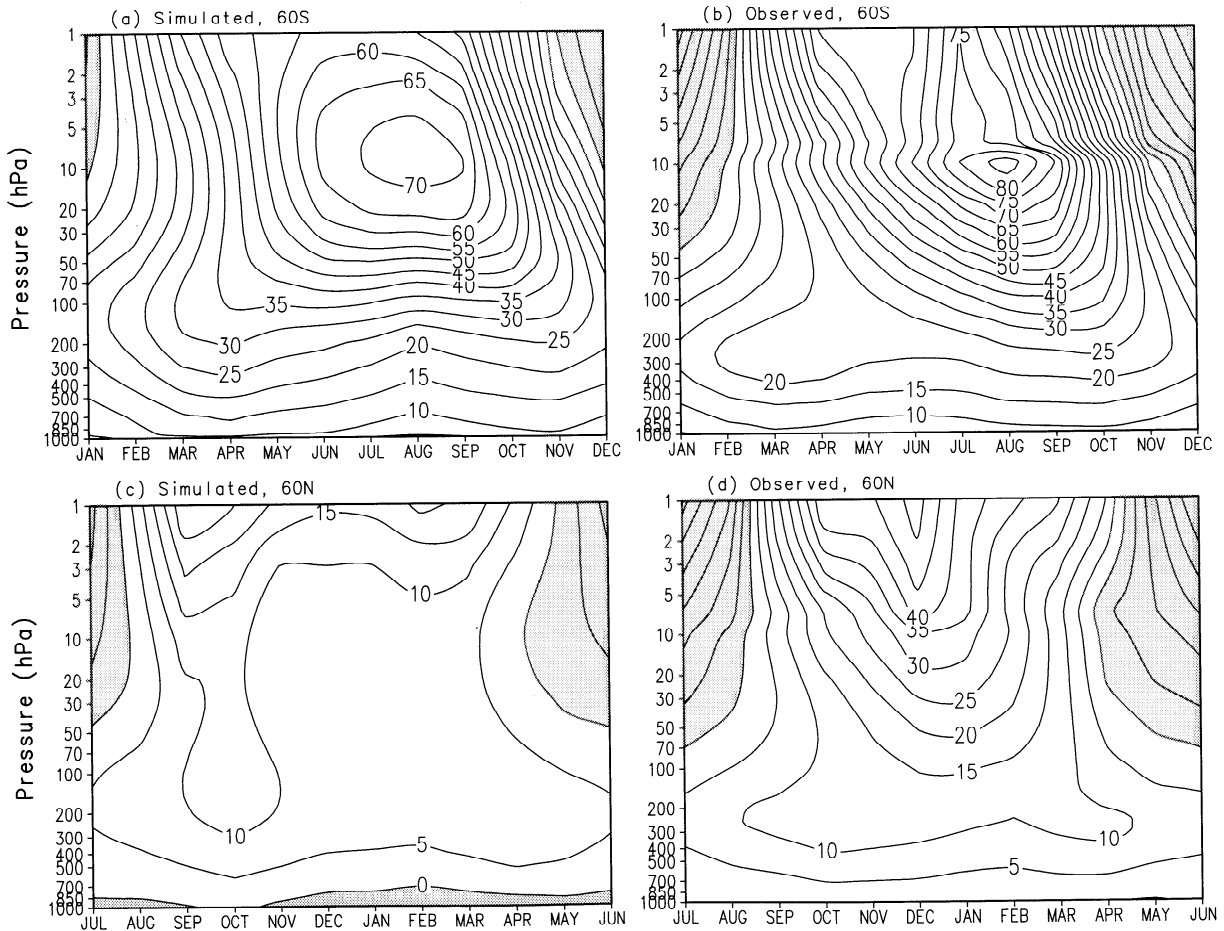
Figure 16. Annual march of monthly mean zonal-mean zonal wind for the simulated model climatology at (a) 60°S and (c) 60°N, and the observed climatology at (b) 60°S and (d) 60°N. The time axis runs from January to December at 60°S and from July to June at 60°N. The contour interval is 5 m s^{-1}. Easterly winds are shaded.
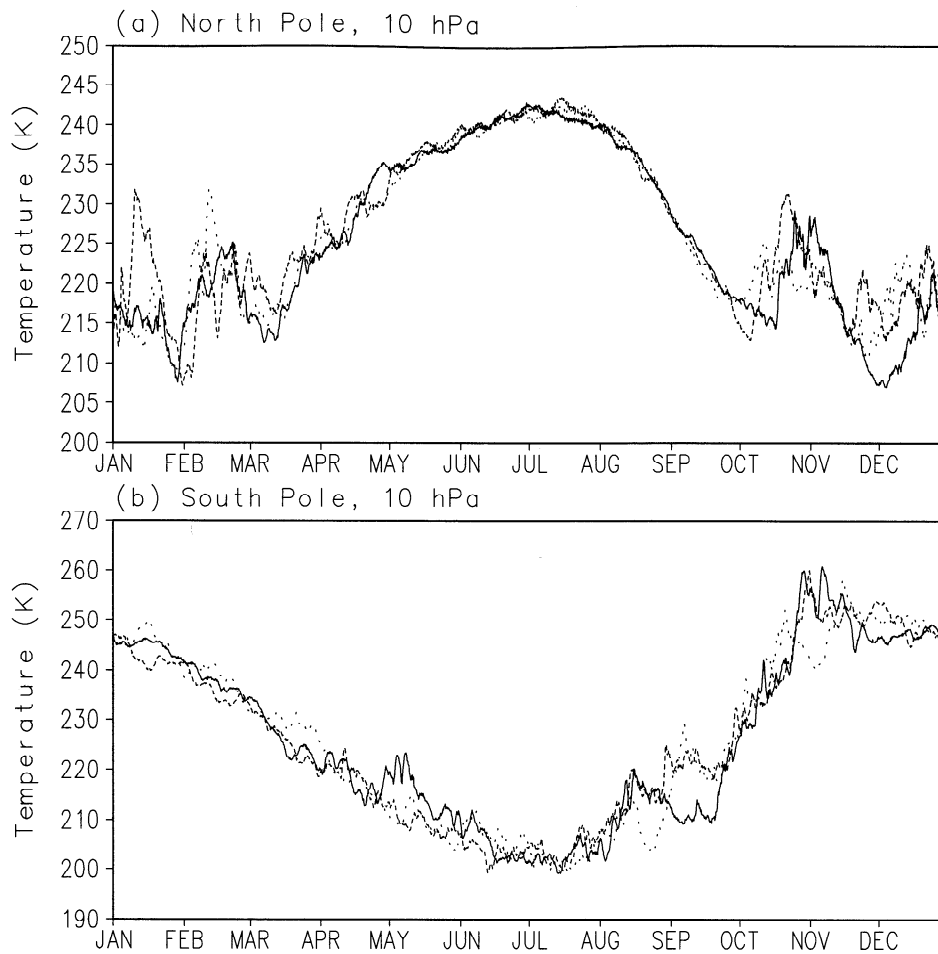
Figure 17. Temperatures (K) at 10 hPa at the North Pole and South Pole sampled at 6-hour intervals for 3 simulated years. Each curve represents 1 year of simulation.

time-latitude distributions of zonal-mean temperature and zonal wind at 10 hPa, sampled at 6-hour intervals for the 3 model years. A 13-point (~ 3 day) running-mean smoothing has been applied to the data before plotting. From ~ 60°N to the North Pole, synoptic-scale variations of temperature occur frequently from late October to late March in all 3 years. The polar-night jet breaks down, and easterly winds build near the North Pole occasionally. In their comparison of sudden warmings simulated by the ECHAM3.5 GCM with observations, *Manzini and Bengtsson* [1996] used the following criteria in selecting major and minor sudden warming events: (1) a minor warming day requires that the meridional temperature gradient at 10 hPa between the North Pole and 60°N be positive and (2) a major warming day requires not only a positive temperature gradient but also easterly winds at 60°N. A warming event must last at least 4 days. They found from a 15-year NMC-CAC analysis that almost no warmings exist before January; minor warmings occur at the highest frequency of days in March (35.9%), and major warmings occur in April (24%). Usually, the breakdown of the polar-night vortex follows the last major warming. Figure 18 shows that the 24-L ST-GCM generates too many warmings, especially in early winter. Consequently, the modeled northern polar-night vortex is weaker and the seasonal-mean temperature is ~ 5°–10°C warmer than

observed (see Figure 13). The westerly winds start to decay in early winter and do not intensify and propagate further downward (see Figure 16). In the Southern Hemisphere the model simulates fairly realistically the variations of temperature and zonal wind.

3.2.5. Equatorial zonal wind. QBO and the semiannual oscillation (SAO) are the most intriguing features of the observed tropical atmospheric circulation. While most GCMs show the ability to simulate the SAO, it is still a great challenge for GCMs to capture even such basic features of the QBO as its amplitude, period, and vertical structure. *Hamilton et al.* [1995], *Horinouchi and Yoden* [1998], *Takahashi and Shiobara* [1995], and *Takahashi* [1999] reported some recent success in simulating the QBO using simplified GCMs.

Figure 19 shows the march of the simulated monthly mean zonal-mean zonal wind at the equator in the stratosphere for 5 years simulated by the UIUC 24-L ST-GCM. The SAO near the stratopause is fairly realistic. The easterly wind has its first maximum in January near 1 hPa and its second maximum in July at a lower altitude near 3 hPa. The westerly wind has maxima in April and October, centered at 2 hPa. Both the easterly and westerly phases have prominent downward-phase propagation similar to the observations. Given the model top at 1 hPa and the momentum damping applied to the
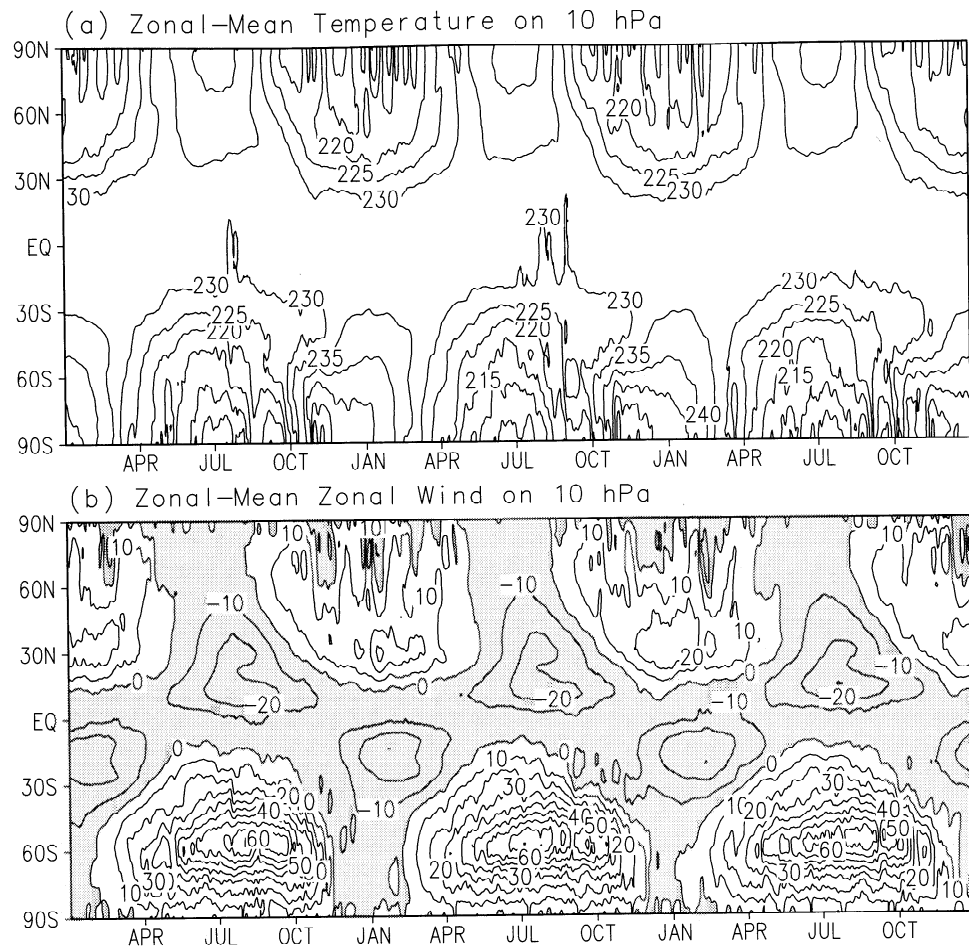
Figure 18. Time-latitude distributions of the (a) simulated zonal-mean temperature (K) and (b) zonal wind (m s^{-1}) at 10 hPa sampled at 6-hour intervals for 3 simulated years. Before plotting, a 13-point filtering (~3 days) has been applied. The contour interval is 5 K for temperature and 10 m s^{-1} for wind. Easterly winds are shaded.
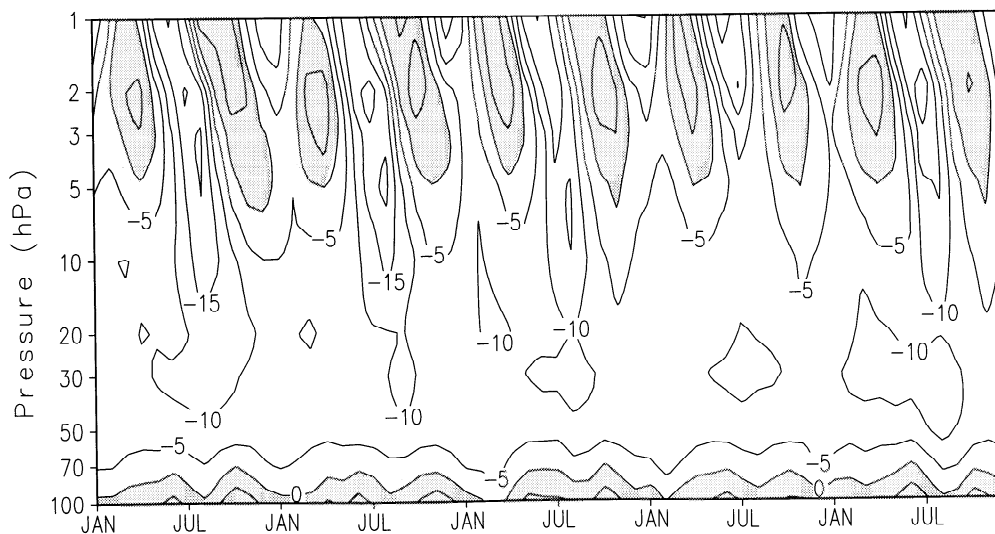

Figure 19. March of the simulated monthly mean zonal-mean zonal wind at the equator for 5 simulated years. The contour interval is 5 m s^{-1}. Westerly winds are shaded.

topmost model layer, the oscillation seems to be centered at a little lower altitude than observed, and its strength is also weaker. Not surprisingly, the UIUC 24-L ST-GCM did not succeed in simulating the QBO, most likely because the model's horizontal and vertical resolutions are too coarse to simulate well the vertical momentum transport by small-scale gravity waves.

3.3. Residual Circulation and Eliassen-Palm Flux Divergence in the Stratosphere

To diagnose the simulated mean-meridional circulation from a Lagrangian point of view and the interactions between the zonal-mean zonal wind and eddy disturbances, we present the simulated residual meridional and vertical winds from the framework of the Transformed Eulerian Mean (TEM) circulation in the stratosphere [*Andrews and McIntyre*, 1976], together with a diagnosis of the zonal momentum tendency in terms of the divergence of the Eliassen-Palm (EP) flux. For two reasons the analysis was performed only for the stratosphere. First the integration of the model is performed for sigma (σ) layers, and the model outputs are transformed onto standard isobaric (p) surfaces. Interpolation of variables, especially eddy fluxes, from σ-layers to p surfaces might introduce large errors in the troposphere because these two coordinate surfaces often cross each other with large angles in the troposphere. Second we saved only the temperature and its product with the winds during the model integration. To perform the TEM calculation we need to convert temperature and the meridional temperature flux into potential temperature and the meridional potential temperature flux. In the troposphere, isothermal and isentropic surfaces have almost opposite slopes, especially in the midlatitudes. Using temperature and the meridional temperature flux on isobaric surfaces to produce potential temperature and the meridional potential temperature flux by simply multiplying them by $(p_0/p)^\kappa$ would introduce large errors, especially for the eddy fluxes. However, the above problems do not occur in the stratosphere because the σ and isobaric surfaces are almost parallel to each other, and isentropic surfaces are also almost parallel to isobaric surfaces.

We performed our analysis using eddy fluxes of momentum and potential temperature sampled at 6-hour intervals and the monthly means of other quantities on the 22 isobaric surfaces of the standard model output (1000, 925, 850, 700, 600, 500, 400, 300, 250, 200, 150, 100, 70, 50, 30, 20, 10, 7, 5, 3, 2, and 1 hPa). For each of the 12 simulated years, the monthly mean residual circulation and EP-flux divergence were derived. Then ensemble seasonal means averaged over the 12 simulated years were calculated. Latitude-height cross sections of the ensemble residual meridional velocity $[\bar{v}]_r$ and residual vertical velocity $[\bar{w}]_r$ for the DJF and JJA seasons are presented in Figure 20, together with the mass streamfunction of the residual circulation. An approximation, $[\bar{\omega}]_r = -[\bar{\rho}]g[\bar{w}]_r$, has been used to convert the vertical velocity $[\omega]_r$ in Pascal/s in p coordinate to $[\bar{w}]_r$ in cm s^{-1} in z coordinate, where $[\bar{\rho}]$ is the monthly mean zonal-mean air density. The mass streamfunction of the residual circulation is calculated by integrating $[\bar{v}]_r = g/(2\pi R_e \cos\phi)\, \partial\psi/\partial p$ from the top of the model, where $\psi = 0$, to 100 hPa. Positive values indicate clockwise motion. We set the North Pole on the right-hand side in Figure 20, contrary to the convention of the other figures in this paper, to compare with published results.

We compare the simulated residual meridional and vertical velocities with those in Figures 6 and 7 of *Coy and Swinbank* [1997] who used the stratospheric data-assimilation systems of the Goddard Space Flight Center (GSFC) and the U.K. Meteorological Office (UKMO). It should be noted that (1) the model configurations are different among the UIUC 24-L ST-GCM and the two assimilation systems used by *Coy and Swinbank* [1997]; (2) *Coy and Swinbank* [1997] presented the residual circulation only for 1992, while we present here a 12-year average; (3) the UKMO and GSFC assimilation systems used different insertion methods for the observed data; and (4) the UKMO assimilation ran once per day, while the GSFC assimilation ran at 6-hour intervals. The diagnosis of model output here is based on 6-hourly sampling. Since the calculations of the residual circulation are based on eddy fluxes, these differences might affect the comparability. Therefore the following comparison is only qualitative.

In the stratosphere, in comparison with the two assimilations, the UIUC 24-L ST-GCM reproduces reasonably well the two-cell Brewer-Dobson circulation in both DJF and JJA, that is, one stronger branch of motion toward the winter pole and another weaker branch of motion toward the summer pole. The observed seasonal reversal of the pole-to-pole circulation near the stratopause is simulated. The simulated $[\bar{v}]_r$ resembles more closely the GSFC assimilation than the UKMO assimilation. Near the stratopause in each season, a primary maximum of the residual meridional velocity $[\bar{v}]_r$ of ~ 1 m s^{-1} appears in the tropics, and a secondary maximum appears in the high latitudes in the winter hemisphere. The UKMO assimilation produces the strongest $[\bar{v}]_r$, and the maxima of $[\bar{v}]_r$ in the winter hemisphere near the stratopause are closer to the poles than are those of the GSFC assimilation and the UIUC 24-L ST-GCM. One noticeable difference between these two assimilations is the near-pole "breaks" of mass transport. In the middle stratosphere the GSFC assimilation produces a weak northward transport in the high latitudes of the Southern Hemisphere and a southward transport in the high latitudes of the Northern Hemisphere. The UKMO assimilation does not have these transports. Figures 20a and 20e show that the UIUC 24-L ST-GCM simulates rather weak "breaks."

Coy and Swinbank [1997] derived the residual vertical velocity $[\bar{w}]_r$ indirectly using $[\bar{v}]_r$ based on the TEM mass continuity equation. We calculated $[\bar{w}]_r$ directly from the vertical velocity and the eddy flux of potential temperature. The diagnosed $[\bar{w}]_r$ agrees with the two assimilations in general, with ascending motion in the summer hemisphere and descending motion in the winter hemisphere. Their magnitudes are also comparable.

To understand the contribution of the "model-resolved" eddy disturbances to the maintenance of the zonal-mean zonal wind, we diagnosed the Eliassen-Palm (EP) flux divergences (ms^{-1} d^{-1}) and present them in Figures 20d and 20h. Both stationary eddies and transient eddies are included in the EP-flux divergences. In the middle to upper stratosphere in both DJF and JJA, strong easterly forcing exists in the winter hemisphere high latitudes, very weak easterly forcing in the summer hemisphere, and weak westerly forcing in the tropics and polar-night regions. The forcing in the upper stratosphere qualitatively matches those simulated by the two mesospheric GCMs, the MACCM2 T42xL21 [*Boville*, 1995], and the Berlin TSM-GCM [*Langematz and Pawson*, 1997]. In the lower stratosphere, in comparison with those two
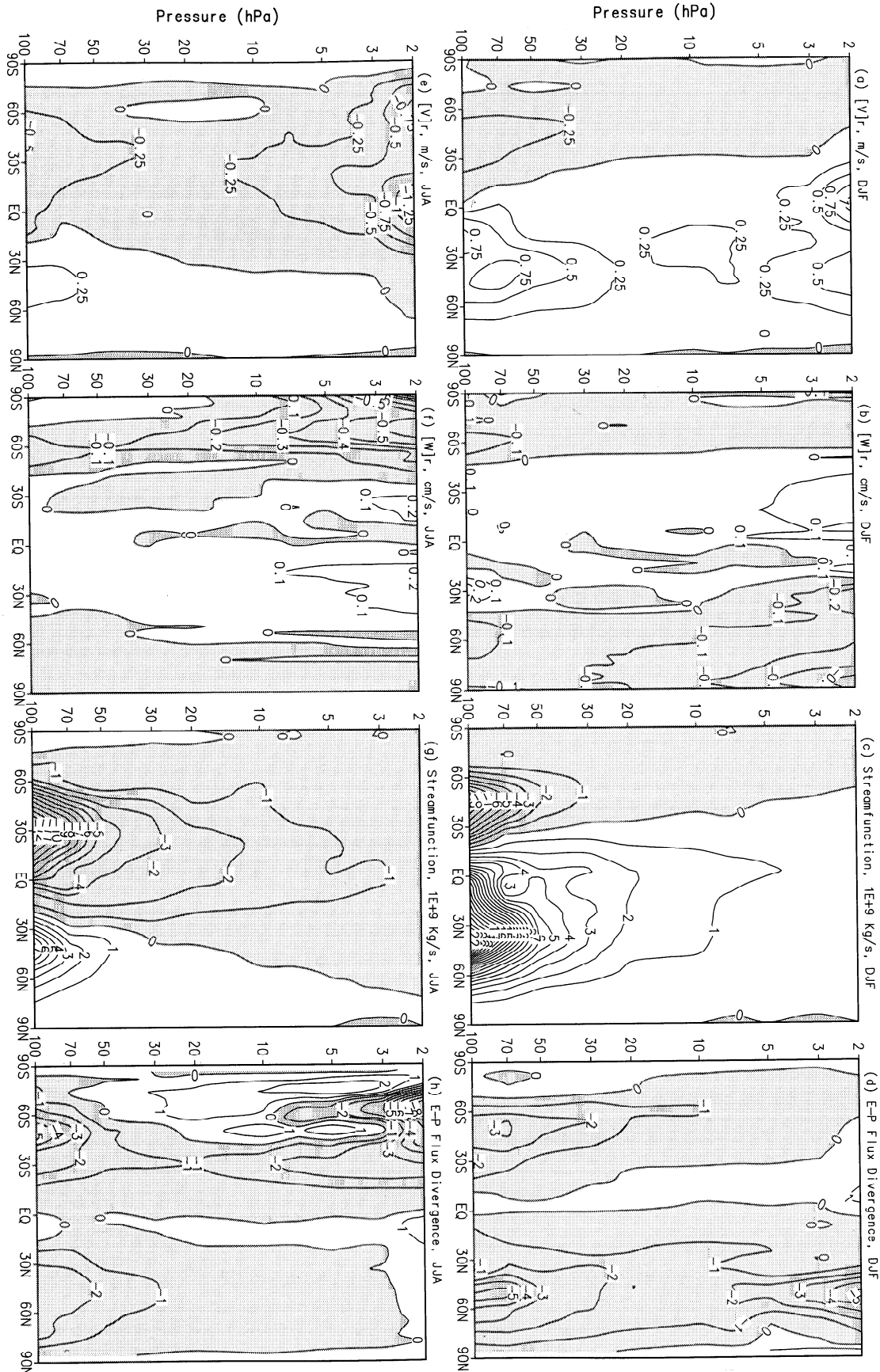
Figure 20. Ensemble residual meridional velocity (m s^{-1}) in (a) and (e), residual vertical velocity (cm s^{-1}) in (b) and (f), mass streamfunction of the residual circulation (10^9 kg s^{-1}) in (c) and (g), and forcing of the zonal-mean zonal wind by the model-resolved eddies in terms of the E-P flux divergence (ms^{-1} d^{-1}) in (d) and (h). Figures 20a-20d are for DJF, and the Figures 20e-20h are for JJA. Negative values are shaded.

mesospheric GCMs, the UIUC 24-L ST-GCM seems to generate stronger easterly forcing in both hemispheres in DJF and JJA.

It should be pointed out that sponge-layer friction, which has been widely used in middle atmosphere models, usually has a large influence on the simulated temperature and circulation in the upper portion of a model [*Shepherd et al.*, 1996]. The UIUC 24-L ST-GCM uses *Hansen et al.*'s [1983] momentum damping on only the topmost layer and has its top at 1 hPa. The MACCM2 [*Boville*, 1995] and the Berlin TSM-GCM [*Langematz and Pawson*, 1997] both use Rayleigh friction on more than one model layer and extend up to 0.01 hPa and 0.0068 hPa, respectively. Thus caution is needed when comparing the EP flux divergences in the upper stratosphere diagnosed from the three models.

4. Summary and Discussion

In this paper we have introduced the UIUC 24-layer stratospheric-tropospheric general circulation model. Compared to its ancestors, the model has a finer vertical resolution and extends higher to the stratopause. New schemes were adopted and developed for the transfer of terrestrial and solar radiation, the interaction between clouds and radiation was revised, the radiative effect of aerosols in both the troposphere and stratosphere was included, and the *Palmer et al.* [1986] parameterization of orographically excited subgrid-scale gravity wave drag was implemented with modifications. The new parameterization for terrestrial radiation takes into account the Doppler broadening of the absorption lines for water vapor, CO_2, and O_3 in the upper stratosphere. Calculations by column radiative-transfer models show that the new terrestrial radiation routine improves the cooling rates in both the troposphere and stratosphere, and the new solar radiation routine yields generally better heating rates in the upper stratosphere. The inclusion of the orographic-type GWD parameterization improves the simulated tropospheric subtropical jets and sea level pressure in both hemispheres; however, it weakens the polar-night jet in the Northern Hemisphere.

To validate the model, a 15-year control simulation was performed with climatological SST and sea-ice extent. The simulated geographical distributions and seasonal variations of surface-air temperature, precipitation, cloud cover, and cloud radiative forcing were compared with observations. The model simulates well the surface-air temperature over the globe, except near the poles. The observed geographical distribution of precipitation was simulated reasonably well. The seasonal variation of the heavy precipitation in the tropics associated with the ITCZ was captured. The simulated cloud cover generally matches the observed, except in the high latitudes of the Southern Hemisphere, where the simulated cloud cover is ~ 20–30% less than observed. It has been found that the scheme used to diagnose the large-scale fractional cloud [*Sundqvist*, 1978, 1988] in the model is very sensitive to relative humidity. The simulation of cloud cover in the high latitudes and near the poles was improved by modifying this scheme. The model simulates well the clear-sky TOA OLR and TOA net incoming solar radiation, except that it systematically underestimates the clear-sky planetary albedo. Under cloudy sky, the model simulates well the observed geographical distribution and seasonal variation of the LW CRF, especially in the tropics. It is found that the LW

CRF in the tropics largely depends on the height of convective clouds, which in turn depends on the threshold relative humidity that controls the onset of penetrating convection in the model [*Wang and Schlesinger*, 1999]. For the SW CRF the model captured its observed geographical distribution and seasonal variation in general. The model overestimated the SW CRF in the tropics and subtropics and underestimated the SW CRF in high latitudes. The largest bias occurred near 60°S in January because of the inaccurately simulated cloud cover. Over the warm pool the simulated absorption of solar radiation by clouds is 35 W m^2 smaller than the ERBE satellite observation.

The simulated atmospheric temperature and circulation were also diagnosed. The model simulates well the observed position of the tropical tropopause, the tropospheric temperature gradients in the middle latitudes, and the subtropical jet streams. In the stratosphere the observed distributions of pole-to-pole temperature gradient in JJA and DJF are captured, and the polar-night jet in the Southern Hemisphere has its observed strength and position. The model also captured the location and phase of the observed semiannual oscillation near the stratopause. Stratospheric sudden warmings were also simulated in the northern middle stratosphere. However, a number of deficiencies exist. The model has a colder-than-observed lower polar stratosphere. In SON and DJF the model is ~ 5°–15°C warmer than observed in the middle and upper polar stratosphere of the Northern Hemisphere. In MAM and JJA the model is ~ 5°–20°C warmer than observed in the southern upper polar stratosphere. The simulated northern polar-night jet is too weak compared to observations and the jet core is shifted equatorward. The simulated southern polar vortex is also a little weaker than observed. The warm bias and the weak polar vortex in the Northern Hemisphere have not been observed in most other GCMs, which usually simulate systematic cold biases and over-intensified polar vortexes. Sensitivity studies in section 2.2.5 indicate that the warm bias in the 24-L ST-GCM is related to the use of the Palmer orographic GWD parameterization.

The analysis of the residual circulation indicates that the model simulates reasonably well the observed two-cell Brewer-Dobson circulation in the stratosphere and its reversal between the two solstice seasons. The model generates easterly forcing by the model-resolved eddies in the middle to upper stratosphere in winter hemispheres, comparable to those simulated by mesospheric GCMs. However, the forcing in the lower stratosphere is too strong.

In this paper, attention has been paid to the warm bias in the polar-night regions and the weak circumpolar vortex in the middle-to-upper polar stratosphere of the Northern Hemisphere. To improve the model's performance, we are currently testing other parameterization schemes on subgrid-scale orographic and nonorographic gravity wave drag. We have also developed a 36-layer mesospheric version of the GCM, which has its top at 0.01 hPa, to investigate the influence of the mesosphere on the simulated northern polar-night jet in the stratosphere. In this mesospheric GCM, Rayleigh friction [*Boville*, 1986] is used above 10 hPa, and the GWD parameterization of *Palmer et al.* [1986] is used below 10 hPa. Preliminary results obtained from perpetual-January simulations show that the warm bias in the northern middle to upper polar stratosphere in the 24-L ST-GCM becomes a cold bias in this mesospheric GCM, and the

northern polar-night jet in the lower stratosphere between 100 hPa and 10 hPa becomes much stronger, with the jet core located approximately at the observed position. The interactions between the mesosphere and stratosphere and the influence of the combined use of Rayleigh friction and orographic GWD parameterizations on the simulated northern polar-night jet of this mesospheric GCM will be further explored.

In summary, compared to its ancestors the UIUC 24-L ST-GCM has significantly improved the simulation in the troposphere and near the surface. It also simulates reasonably well the stratospheric temperature and circulation, except the northern polar-night jet. To further develop the model, special attention should be paid to the simulation of cloud cover and the parameterization of the subgrid-scale gravity wave drag. The simulated radiative forcing and many tropospheric variables largely depend on the spatial distributions of cloudiness. A better GWD parameterization is expected to be able to significantly improve the simulation in the stratosphere.

References

Alexander, M.J., and T.J. Dunkerton, A spectral parameterization of mean-flow forcing due to breaking gravity waves, *J. Atmos. Sci.*, *56*, 4167-4182, 1999.

Andrews, D.G., and M.E. McIntyre, Planetary waves in horizontal and vertical shear: The generalized Eliassen-Palm relation and the mean zonal acceleration, *J. Atmos. Sci.*, *33*, 2031-2048, 1976.

Andronova, N.G., E. Rozanov, F. Yang, M.E. Schlesinger, and G.L. Stenchikov, Radiative forcing by volcanic aerosols from 1850 through 1994, *J. Geophys. Res.*, *104*, 16,807-16,826, 1999.

Arakawa, A., Computational design for long-term numerical integration of the equations of fluid motion: Two dimensional incompressible flow, Part I, *J. Comput. Phys.*, *1*, 119-143, 1966.

Arakawa, A., Parameterization of cumulus convection, paper presented at WMO/IUGG Symposium on Numerical Weather Prediction, Jpn. Meteorol. Agency, Tokyo, November 26 to December 4, 1969.

Arakawa, A., and V.R. Lamb, Computational design of the basic dynamical processes of the UCLA general circulation model, in *Methods in Computational Physics*, edited by J. Chang, pp. 173-265, Academic, San Diego, Calif., 1977.

Arakawa, A., and Y. Mintz, The UCLA atmospheric general circulation model, paper presented at Workshop on The UCLA Atmospheric General Circulation Model, Univ. Calif. Los Angeles, Department of Meteorol., Los Angeles, 1974.

Arakawa, A., and W.H. Schubert, Interaction of a cumulus cloud ensemble with the large scale environment, Part I, *J. Atmos. Sci.*, *31*, 674-701, 1974.

Beagley, S.R., J. de. Grandpre, J.N. Koshyk, N.A. McFarlane, and T.G. Shepherd, Radiative-dynamical climatology of the first-generation Canadian middle atmosphere model, *Atmos. Ocean*, *35*, 293-331, 1997.

Boucher, O., and U. Lohmann, The sulfate-CCN-cloud albedo effect, *Tellus, Ser. B*, *47B*, 281-300, 1995.

Boucher, O., et al., Intercomparison of models representing direct shortwave radiative forcing by sulfate aerosols, *J. Geophys. Res.*, *103*, 16,979-16,998, 1998.

Boville, B.A., Wave-mean flow interactions in a general circulation model of the troposphere and stratosphere, *J. Atmos. Sci.*, *43*, 1711-1714, 1986.

Boville, B.A., Middle atmosphere version of CCM2 (MACCM2): Annual cycle and interannual variability, *J. Geophys. Res.*, *100*, 9017-9039, 1995.

Briegleb, B.P., and V. Ramanathan, Spectral and diurnal variation in clear-sky planetary albedo, *J. Appl. Meteorol.*, *21*, 1160-1171, 1982.

Briegleb, B.P., P. Minnis, V. Ramanathan, and E. Harrison, Comparison of regional clear-sky albedo inferred from satellite observation and model computations, *J. Clim. Appl. Meteorol.*, *25*, 214-226, 1986.

Cess, R.D., et al., Absorption of solar radiation by clouds: Observations versus models, *Science*, *267*, 496-499, 1995.

Cess, R.D., et al., Comparison of the seasonal change in cloud-radiative forcing from atmospheric general circulation models and satellite observations, *J. Geophys. Res.*, *102*, 16,593-16,603, 1997.

Chou, M.D., Parameterizations for the absorption of solar radiation by O_2 and CO_2 with application to climate studies, *J. Clim.*, *3*, 209-217, 1990.

Chou, M.D., A solar radiation model for use in climate studies, *J. Atmos. Sci.*, *49*, 762-772, 1992.

Chou, M.D., and K.T. Lee, Parameterizations for the absorption of solar radiation by water vapor and ozone, *J. Atmos. Sci.*, *53*, 1203-1208, 1996.

Chou, M.D., and M.J. Suarez, An efficient thermal infrared radiation parameterization for use in General Circulation Models, in *Technical Report Series on Global Modeling and Data Assimilation*, v.3, 85 pp., NASA Greenbelt, Md., 1994.

Chou, M.D., and M.J. Suarez, A solar radiation parameterization for atmospheric studies, in *Technical Report Series on Global Modeling and Data Assimilation*, v.15, 40 pp., NASA Greenbelt, Md., 1999.

Coy, L., and R. Swinbank, Characteristics of stratospheric winds and temperature produced by data assimilation, *J. Geophys. Res.*, *102*, 25,763-25,781, 1997.

Cullen, M.J.P., The unified forecast/climate model, *Meteorol. Mag.*, *122*, 81-93, 1993.

Doronin, Y.P., *Thermal Interaction of the Atmosphere and the Hydrosphere in the Arctic*, 244 pp., Israel Prog. for Sci. Transl., Jerusalem, 1969.

Fiedler, F., and M.A. Panofsky, The geostrophic drag coefficient and the "effective" roughness length, *Q. J. R. Meteorol. Soc.*, *98*, 212-220, 1972.

Gates, W.L., and A.B. Nelson, A new (revised) tabulation of the Scripps topography on a one-degree grid, Part 1, Terrain heights, Tech rep. R-1276-1-ARPA, 132 pp., Rand Corp., Santa Monica, Calif., 1975.

Gates, W.L., E.S. Batten, A.B. Kahle, and A.B. Nelson, A documentation of the Mintz-Arakawa two-level atmospheric general circulation model, R-877-ARPA, 408 pp., Rand Corp., Santa Monica, Calif., 1971.

Ghan, S.J., J.W. Lingaas, M.E. Schlesinger, R.L. Mobley, and W.L. Gates, A documentation of the OSU two-level atmospheric general circulation model, rep. 35, 395 pp., Clim. Res. Inst., Oregon State Univ., Corvallis, 1982.

Gleckler, P., AMIP Newsletter: WGNE Atmospheric Model Intercomparison Project, vol.9, 8 pp., Atmos. Model Intercomparison Proj., Livermore, Calif., 1999.

Gregory, D., G.J. Shutts, and J.R. Mitchell, A new gravity-wave-drag scheme incorporating anisotropic orography and low-level wave breaking: Impact upon the climate of the UK Meteorological Office Unified Model, *Q. J. R. Meteorol. Soc.*, *124*, 463-493, 1998.

Griffith, K.T., S.K. Cox, and R.C. Knollenberg, Infrared radiative properties of tropical cirrus clouds inferred from aircraft measurements, *J. Atmos. Sci.*, *37*, 1073-1083, 1980.

Guinn, T. A., and W.H. Schubert, Stratus: An interactive mixed layer model for personal computers (version 1.0), Dep. of Atmos. Sci., Colorado State Univ., Fort Collins, 1989.

Hamilton, K., Gravity wave process and their parameterization in global climate models, paper presented at NATO Advanced Research Workshop, Santa Fe, N. M., April 1-5, 1996.

Hamilton, K., R.J. Wilson, J.D. Mahlman, and L.J. Umscheid, Climatology of the SKYHI troposphere-stratosphere-mesosphere general circulation model, *J. Atmos. Sci.*, *52*, 5-43, 1995.

Hansen, J., G. Russell, D. Rind, P. Stone, A. Lacis, S. Lebedeff, R.

Ruedy, and L. Travis, Efficient three-dimensional global models for climate studies: Models I and II, *Mon. Weather Rev.*, *111*, 609-662, 1983.

Hines, C.O., Doppler-spread parameterization of gravity-wave momentum deposition in the middle atmosphere, Part 1, Basic formulation, *J. Atmos. Terr. Phys.*, *59*, 371-386, 1997a.

Hines, C.O., Doppler-spread parameterization of gravity-wave momentum deposition in the middle atmosphere, Part 2, Broad and quasi-monochromatic spectra, and implementation, *J. Atmos. Terr. Phys.*, *59*, 387-400, 1997b.

Horinouchi, T., and S. Yoden, Wave mean flow interaction associated with a QBO-like oscillation in a simplified GCM, *J. Atmos. Sci.*, *55*, 502-526, 1998.

Houghton, J. T., L.G. Meira Filho, B. A. Callander, N. Harris, A. Kattenberg, and K. Maskell (Eds.), *Climate Change 1995: The Science of Climate Change*, 572 pp., Cambridge Univ. Press, New York, 1996.

Kiehl, J.T., and B.P. Briegleb, The relative roles of sulfate aerosols and greenhouse gases in climate forcing, *Science*, *260*, 311-314, 1993.

King, M.D., and Harshvardhan, Comparative accuracy of selected multiple scattering approximations, *J. Atmos. Sci.*, *43*, 784-801, 1986.

Kuo, Y.H., Further studies of the parameterization of the influence of cumulus convection of large-scale flow, *J. Atmos. Sci.*, *31*, 1232-1240, 1974.

Langematz, U., and S. Pawson, The Berlin troposphere-stratosphere-mesosphere GCM: Climatology and forcing mechanisms, *Q. J. R. Meteorol. Soc.*, *123*, 1075-1096, 1997.

Langner, J., and H. Rodhe, A global three dimensional model of the tropospheric sulfur cycle, *J. Atmos. Chem.*, *13*, 225-263, 1991.

Lilly, D.K., Models of cloud-topped mixed layers under a strong inversion, *Q. J. R. Meteorol. Soc.*, *94*, 292-309, 1968.

Lindzen, R.S., Turbulence and stress owing to gravity wave and tidal breakdown, *J. Geophys. Res.*, *86*, 9709-9714, 1981.

Manabe, S.J., J.S. Smagorinsky, and R.F. Strickler, Simulated climatology of a general circulation model with a hydrological cycle, *Mon. Weather Rev.*, *93*, 769-798, 1965.

Manzini, E., and L. Bengtsson, Stratospheric climate and variability from a general circulation model and observations, *Clim. Dyn.*, *12*, 615-639, 1996.

Matthews, E., Global vegetation and land use: New high-resolution data bases for climate studies, *J. Clim. Appl. Meteorol.*, *22*, 474-487, 1983.

McClatchey, R.A., R.W. Fenn, J.E.A. Selby, F.E. Volz, and J.S. Garing, *Optical Properties of the Atmosphere*, 3rd ed., 108 pp., Air Force Cambridge Res. Lab., Bedford, Mass., 1972.

McFarlane, N.A., The effect of orographically excited gravity wave drag on the general circulation of the lower stratosphere and troposphere, *J. Atmos. Sci.*, *14*, 1775-1800, 1987.

Medvedev, A.S., and G.P. Klaassen, Vertical evolution of gravity wave spectra and the parameterization of associated wave drag, *J. Geophys. Res.*, *100*, 25,841-25,853, 1995.

Medvedev, A.S., G.P. Klaassen, and S.R. Beagley, On the role of an anisotropic gravity wave spectrum in maintaining the circulation of the middle atmosphere, *Geophys. Res. Lett.*, *25*, 509-512, 1998.

Monteith, J.L., *Principles of Environmental Physics*, 236 pp., Edward Arnold, London, 1973.

Oh, J.H., Physically-based general circulation model parameterization of clouds and their radiative interaction, Ph. D. dissertation, 315 pp., Oregon State Univ., Corvallis, 1989.

Palmer, T.N., G.J. Shutts, and R. Swinbank, Alleviation of a systematic westerly bias in general circulation and numerical weather prediction models through an orographic gravity wave drag parameterization, *Q. J. R. Meteorol. Soc.*, *112*, 1001-1039, 1986.

Ramanathan, V., B. Subasilar, G.J. Zhang, W. Conant, R.D. Cess, J.T. Kiehl, H. Grassl, and L. Shi, Warm pool heat budget and shortwave cloud forcing: A missing physics?, *Science*, *267*, 499-503, 1995.

Rees, D., J.J. Barnett, and K. Labitzke, COSPAR international reference atmosphere: 1986, Part II, Middle atmosphere models, *Adv. in Spaces Res.*, *10*(12), 519 pp., 1990.

Rind, D., R. Suozzo, and N.K. Balarchandran, The GISS global climate-middle atmosphere model, Part II, Model variability due to interactions between planetary waves, the mean circulation, and gravity wave drag, *J. Atmos. Sci*, *45*, 371-386, 1988a.

Rind, D., R. Suozzo, N.K. Balarchandran, A. Lacis, and G. Russell, The GISS global climate-middle atmosphere model, Part I, Model structure and climatology, *J. Atmos. Sci.*, *45*, 329-370, 1988b.

Rossow, W.B., L.C. Garder, P.J. Lu, and A.W. Walker, *International Satellite Cloud Climatology Project (ISCCP) Documentation Of Cloud Data*, 76 pp., World Meteorol. Org., Geneva, 1991.

Rozanov, E., V. Zubov, M.E. Schlesinger, F. Yang, and N. Andronova, Three-dimensional simulations of ozone in the stratosphere and comparison with UARS data, *Phys. Chem. Earth*, *24*, 459-463,1999a.

Rozanov, E., V. Zubov, M.E. Schlesinger, F. Yang, and N.G. Andronova, The UIUC three-dimensional stratospheric chemical transport model: Description and evaluation of the simulated source gases and ozone, *J. Geophys. Res.*, *104*, 11,755-11,781, 1999b.

Schlesinger, M.E., and J.-H. Oh, A cloud evaporation parameterization for general circulation models, *Mon. Weather Rev.*, *121*, 1239-1248, 1993.

Schlesinger, M.E., and M. Verbitsky, Simulation of glacial onset with a coupled atmospheric general circulation/mixed-layer ocean–ice-sheet/asthenosphere model, *Palaeoclimates Data Modell.*, *2*, 179-201, 1996.

Schlesinger, M.E., and Z.-C. Zhao, Seasonal climate changes induced by doubled CO_2 as simulated by the OSU atmospheric GCM/mixed-layer ocean model, *J. Clim.*, *2*, 459-495, 1989.

Schlesinger, M.E., J.-H. Oh, and D. Rosenfeld, A parameterization of the evaporation of rainfall, *Mon. Weather Rev.*, *116*, 1887-1895, 1988.

Schlesinger, M.E., N.G. Andronova, B. Entwistle, A. Ghanem, N. Ramankutty, W. Wang, and F. Yang, Modeling and simulation of climate and climate change, in *Past and Present Variability of the Solar-Terrestrial System: Measurement, Data Analysis and Theoretical Models*, edited by G. Cini Castagnoli and A. Provenzale, pp. 389-429, IOS Press, Amsterdam, 1997a.

Schlesinger, M.E., N. Andronova, A. Ghanem, S. Malyshev, T. Reichler, E. Rozanov, W. Wang, and F. Yang, Geographical scenarios of greenhouse-gas and anthropogenic-sulfate-aerosol induced climate changes, 86 pp., Dep. of Atmos. Sci., Univ. of Ill. at Urbana-Champaign, 1997b.

Shepherd, T.G., K. Semeniuk, and J.N. Koshyk, Sponge layer feedbacks in middle-atmosphere models, *J. Geophys. Res.*, *101*, 23,447-23,464, 1996.

Slingo, A., A GCM parameterization for the shortwave radiative properties of water clouds, *J. Atmos. Sci.*, *46*, 1419-1427, 1989.

Starr, D.O.C., and S.K. Cox, Cirrus clouds, Part II, Numerical experiments on the formation and maintenance of cirrus, *J. Atmos. Sci.*, *42*, 2682-2694, 1985.

Stephens, G.L., Radiation profiles in extended water clouds, Part II, Parameterization schemes, *J. Atmos. Sci.*, *35*, 2123-2132, 1978.

Sundqvist, H., A parameterization scheme for non-convective condensation including prediction of cloud water content, *Q. J. R. Meteorol. Soc.*, *104*, 677-690, 1978.

Sundqvist, H., Parameterization of condensation and associated clouds in models for weather prediction and general circulation simulation, in *Physically-Based Modelling and Simulation of Climate and Climatic Change, Part 1*, edited by M.E. Schlesinger, pp. 433-462, Kluwer Acad., Norwell, Mass., 1988.

Swinbank, R., W.A. Lahoz, A. O'Neill, C.S. Douglas, A. Heaps, and D. Podd, Middle atmosphere variability in the UK Meteorological Office Unified Model, *Q. J. R. Meteorol. Soc.*, *124*, 1485-1526, 1998.

Takahashi, M., Simulation of the quasi-biennial oscillation in a general circulation model, *Geophys. Res. Lett.*, *26*, 1307-1310, 1999.

Takahashi, M., and M. Shiobara, A note on a QBO-like oscillation in the 1/5 sector CCSR/NIES GCM, *J. Meteorol. Soc. Jpn.*, *73*, 131-137, 1995.

Tokioka, T., Some consideration on vertical differencing, *J. Meteorol. Soc. Jpn.*, *2*, 98-111, 1978.

Trenberth, K.E., J.C. Berry, and L.E. Buja, Vertical interpolation and truncation of model-coordinate data, *NCAR/TN-396+STR*, 54 pp., Natl. Cent. for Atmos. Res., Boulder, Colo. 1993.

Vinnikov, K.Y., and I.B. Yeserkepova, Soil moisture: Empirical data and model results, *J. Clim.*, *4*, 66-79, 1991.

Wang, W., Use of the UIUC 11-Layer atmospheric general circulation model to simulate and understand the tropical intraseasonal oscillation, Ph.D. dissertation, 243 pp., Univ. of Illinois at Urbana-Champaign, Urbana, 1996.

Wang, W., and M.E. Schlesinger, The dependence on convective parameterization of tropical intraseasonal oscillations – an assessment using the UIUC GCM, in *Proceedings of the First*

International Atmospheric Model Intercomparison Project (AMIP) Scientific Conference, edited by W. L. Gates, pp. 125-130, World Meteorol. Org., Geneva, 1995.

Wang, W., and M.E. Schlesinger, The dependence on convection parameterization of the tropical intraseasonal oscillation simulated by the 11-layer UIUC atmospheric GCM, *J. Clim.*, *12*, 1423-1457, 1999.

Wang, W.-C., X.-Z. Liang, M.P. Dudek, D. Pollard, and S.L. Thompson, Atmospheric ozone as a climate gas, *Atmos. Res.*, *37*, 247-256, 1995.

Wild, M., A. Ohmura, and H. Gilgen, Validation of general circulation model radiative fluxes using surface observations, *J. Clim.*, *8*, 1309-1323, 1995.

World Climate Research Project SPARC, Stratospheric processes and their relation to climate: SPARC implementation plan, *WCRP-105*, 131 pp., Geneva, 1998.

World Meteorological Organization (WMO), A preliminary cloudless standard atmosphere for radiation computation, *WCP-112*, 58 pp., Int. Assoc. For Meteorol. and Atmos. Phys., Radiation Commission, Geneva, 1986.

Xie, P., and P. Arkin, Global precipitation: A 17-year monthly analysis based on gauge observations, satellite estimates, and numerical model outputs, *Bull. Am. Meteorol. Soc.*, *78*, 2539-2558, 1997.

Yang, F., Radiative forcing and climatic impact of the mount Pinatubo volcanic eruption, Ph.D. dissertation, 219 pp., Univ. of Illinois at Urbana-Champaign, Urbana, 2000.

E. Rozanov, M. E. Schlesinger, and F. Yang, Department of Atmospheric Sciences, University of Illinois at Urbana-Champaign, 105 S. Gregory Street, Urbana, IL 61801. (schlesin@atmos.uiuc.edu)